

UC San Diego

UC San Diego Electronic Theses and Dissertations

Title

Three-Dimensional Left and Right Ventricular Strain Distributions in The Rat Heart /

Permalink

<https://escholarship.org/uc/item/0hr8r5g0>

Author

Barrio, Martin J.

Publication Date

2013

Peer reviewed|Thesis/dissertation

UNIVERSITY OF CALIFORNIA, SAN DIEGO

**THREE-DIMENSIONAL LEFT AND RIGHT VENTRICULAR
STRAIN DISTRIBUTIONS IN THE RAT HEART**

A Thesis submitted in partial satisfaction of the requirements
for the degree Master of Science

in

Bioengineering

by

Martin J. Barrio

Committee in charge:

Professor Jeffrey H. Omens, Chair
Professor Andrew McCulloch, Co-Chair
Professor Thomas Liu

2013

Copyright

Martin J. Barrio, 2013

All rights reserved.

The Thesis of Martin J. Barrio is approved, and it is acceptable in quality and form for publication on microfilm and electronically:

Co-Chair

Chair

University of California, San Diego

2013

TABLE OF CONTENTS

Signature Page.....	iii
Table of Contents.....	iv
List of Figures.....	vii
List of Tables.....	ix
Abstract of the Thesis.....	x
1 Introduction.....	1
1.1 Cardiac Anatomy and Function.....	1
1.2 Ventricular Strain Measurements.....	2
1.3 Finite Element Modeling.....	4
1.4 Harmonic Phase Algorithm.....	6
1.5 Specific Aims.....	6
2 Materials and Methods.....	8
2.1 Animal Preparation.....	8
2.2 Hemodynamic Analysis.....	9
2.3 Cardiac Magnetic Resonance Imaging.....	9
2.3.1 Anatomical and SPAMM Tagged Cine MRI.....	9
2.3.2 Diffusion Tensor MRI.....	12
2.4 Image Analysis.....	12
2.5 Harmonic Phase Algorithm.....	13
2.5.1 Band Pass Filter Selection.....	15
2.5.2 HARP Tracking Algorithm.....	18
2.5.3 Shortest Path Refinement (SP-HARP).....	23

2.1.3.1	Cost Functions.....	23
2.1.3.2	Motion Tracking via SP-HARP.....	25
2.6	Cardiovascular Model.....	27
2.6.1	Anatomical Model.....	28
2.6.1.1	Bi-Ventricular Geometry.....	28
2.6.1.2	Ventricular Fiber Architecture.....	29
2.6.1.3	Mapping the Fiber Architecture to End-Diastolic Models...	30
2.6.2	Lagrangian Strain Analysis.....	31
2.6.3	Preliminary Ventricular Simulations.....	32
2.6.3.1	Passive Material Properties.....	32
2.6.3.2	Active Contraction and Hemodynamic Model.....	33
3	Results.....	36
3.1	Rat Anatomical Model.....	36
3.2	HARP Tracking.....	40
3.3	Three-Dimensional Strain Analysis.....	43
3.4	Preliminary Simulation Results.....	50
4	Discussion.....	52
4.1	HARP Algorithm.....	52
4.2	Anatomical Model.....	53
4.3	Deformation Calculations.....	54
5	Conclusion.....	59
	References.....	61

LIST OF FIGURES

Figure 1-1: Detailed representation of the heart.....	2
Figure 2-1: Example anatomical images taken from a single rat.....	11
Figure 2-2: A sequence of tagged MRI of a rat heart.....	11
Figure 2-3: Example DT-MRI slice performed on a excised rat heart.....	12
Figure 2-4: Example of HARP processing on a single slice.....	15
Figure 2-5: Example of the bandpass filter centered at a frequency w	17
Figure 2-6: An example of the fitted anatomical model with a aligned reconstructed slice from the DT-MRI images before fitting. The slices were aligned with the model and the tensors were rotated as well.....	30
Figure 2-7: A view of the transformation used to reorient the diffusion tensors.	31
Figure 2-8: A representation of the three-element windkessel model.....	34
Figure 2-9: Example exponential fitting on the aortic pressure curve.....	35
Figure 3-1: DT Measurements made on the excised control and hypertensive models.....	37
Figure 3-2: Overlap metric calculation for DT models.....	38
Figure 3-3: Comparison between raw and fitted DT data.....	39
Figure 3-4: Regions of poor overlap between fitted and raw DT data.....	39
Figure 3-5: DT Measurements made on the ED control and hypertensive models...	40
Figure 3-6: HARP tracking results for a control heart axial slice.....	41
Figure 3-7: HARP tracking results for a hypertensive heart axial slice.....	42
Figure 3-8: HARP tracking results for a control heart long axis slice.....	43

Figure 3-9: HARP tracking results for a hypertensive heart long axis slice.....	43
Figure 3-10: End-systolic strain maps for multiple components.....	45
Figure 3-11: Fiber Strain Distribution maps from end-diastole to end-systole for the (A) Control and (B) Hypertensive models.....	46
Figure 3-12: Strain distribution time courses from end-diastole to end-systole for the control and hypertensive heart.....	48
Figure 3-13: Longitudinal strain differences vs. Wall thickness differences for different regions in the LV and RV.....	49
Figure 3-14: Cross-Fiber strain differences vs. Overlap for different regions in the LV and RV.....	49
Figure 3-15: Simulation Results for the control heart.....	51
Figure 3-16: Simulation Results for the hypertensive heart.....	51

LIST OF TABLES

Table 3-1: Three-Dimensional Strain Components in the LV and RV for the Control and Hypertensive Hearts compared to Published Values.....	45
Table 3-2: Windkessel Paramaters for Simulations.....	49

ABSTRACT OF THE THESIS

**THREE-DIMENSIONAL LEFT AND RIGHT VENTRICULAR
STRAIN DISTRIBUTIONS IN THE RAT HEART**

by

Martin J. Barrio

Master of Science in Bioengineering

University of California, San Diego, 2013

Professor Jeffrey H. Omens, Chair

Many studies have shown that strain measurements are becoming viable for diagnostic and clinical purposes. Strain has shown potential in serving as early indicator for a host of cardiac diseases such coronary disease, hypertension, etc. Therefore, it is crucial to develop techniques to accurately determine strain. There are many different

methods to measure cardiac regional mechanics using a variety of techniques such as Doppler echocardiographic imaging as well harmonic phase algorithm (HARP). These methods are popular, as they have produced accurate systolic strains. However, both methods have their limitations. Previous studies have combined HARP with finite element modeling to compute 3D circumferential, radial and longitudinal strains in mice, however they limited their calculations to the left ventricle. Here, we use combine MRI, DT-MRI, and HARP to measure the same distributions, but in addition, we measure fiber, sheet-normal and cross-fiber strains in both the left and right ventricle. In order to examine this structure-function relationship, we will determine regional function in the left and right ventricle using a structure-dependent computational model of cardiac mechanics. Using normotensive and hypertensive rat hearts models, we will quantify the time course of regional strain throughout the left and right ventricle. These measures, along with ECG and blood pressures, will be used as inputs to a finite element model of the contracting ventricles. The goal of these studies will be to determine if these measures are sufficient to produce accurate strain fields in rat hearts.

1 Introduction

1.1 Cardiac Anatomy and Function

The heart is a muscular organ that pumps blood throughout the circulatory system delivering oxygenated blood and removing the waste from other organs. It is composed of four main chambers: the left and right atria (LA, RA) and the left and right ventricles (LV, RV). There are four main valves that direct the blood flow in one direction; two atrioventricular (AV) and two semilunar (SL) valves. The two AV valves are the tricuspid and mitral valve and they are responsible for preventing backflow of blood into the atria. The tricuspid valve is located between the RA and RV and the mitral valve is located between the LA and LV. The two SL valves, aortic and pulmonary valves, are responsible for forcing blood into the arteries as well as prevent backflow into the ventricles. A detailed illustration of the heart is shown in Figure 1-1.

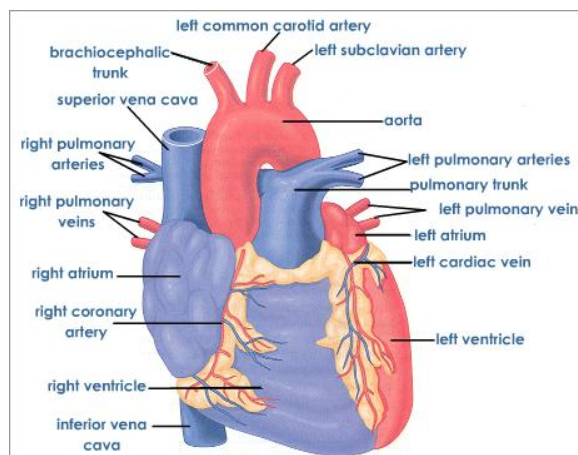


Figure 1-1: Detailed representation of the heart

The cardiac cycle describes the process in which the heart pumps blood to the rest of the body. It can be described in two main stages: diastole and systole. Diastole begins with isovolumic relaxation, where both all the valves remain closed and the atria are filling with blood. It continues until the ventricular pressures fall below the atrial pressures and thus the SL valves will open initiating the filling stage, where the ventricles fill with blood. Diastole ends when the ventricles are completely filled and the myocytes begin to contract, which begins the next stage, systole. The ventricular pressures rise gradually until they exceed either the aorta or the pulmonary artery, which leads to opening of the SL valves and ejection. During this stage, blood flows out of the ventricles into the rest of body. Systole ends when end systolic volume of the heart is reached and when relaxation stage begins again.

1.2 Ventricular Strain Measurements

Measuring ventricular strain measurements is crucial in identifying heart diseases. Higaki et al [20] shows that global two-dimensional strain could be used to detect myocardial fibrosis with patients with normal ventricular function. The group showed

that hypertrophic patients had a significantly lower longitudinal strain compared to the norm. Holt [21] has suggested the use of measuring strain to detect early signs of coronary disease or myocardial infarctions. Studies have shown that longitudinal strain is reduced in patients with infarctions and correlate with the infarct size and ejection fraction [21]. Edvardsen et al. [22] also showed how longitudinal strain can be a great predictor of infarct size in the chronic ischaemic heart disease. Young et al. [23] showed that patients with type two diabetes and left ventricular dysfunction had circumferential and longitudinal strains 14% and 22% smaller, respectively compared to normal patients. Thus, it has been shown in the literature that strain measurements can be a powerful indicator of certain heart diseases, in particular when regional functional indices are important, even in studies that show normal global ventricular function.

Previous studies have focused mostly on calculating two dimensional strain using echocardiograph techniques [20, 21, 22, 23]. These methods have produced accurate rapid systolic strain results and have seen widespread clinical use, however there are a number of limitations. The number of strain components that can be calculated is reduced based on image orientation [24]. Doppler echocardiograph is limited by lack of fixed reference points in the myocardium; therefore sampling the same points throughout the cardiac cycle is not possible [25]. Doppler-derived strains have also been limited due to their poor reproducibility. There are other methods that have used the combination of tagged magnetic resonance imaging (MRI) and harmonic phase algorithm (HARP). HARP has been shown to calculate highly accurate strains [1, 2, 3, 4], however it is limited by the calculation in two dimensions. Standard HARP tracking also requires many frames to track material points as large deformations lead to increased number of

mis-tracked points. Chuang et al. [18] has combined both HARP and finite element modeling to calculate three-dimensional strains, but the group limited their measurements to the left ventricle. Most of these studies focus their strain calculations to circumferential, radial, and longitudinal where the heart fiber architecture is not taken into account. Therefore, they did not possess the ability to calculate fiber, sheet-normal, and cross-fiber strains. It is important to make to calculate these specific strain maps as they have shown to be linked with wall thickening [27].

Thus, the ability to calculate strain maps could be extremely useful to predict heart disease and therefore measuring high accurate three dimensional strain distributions is crucial. In this study, we will combine MRI, HARP, and Diffusion tensor MRI to create finite element models that will be used to calculate circumferential, radial, longitudinal, fiber, sheet-normal, and cross-fiber strain distributions for both the LV and RV.

1.3 Finite Element Modeling

Computation models have shown a tremendous increase in use in the past decade, due to advances in technology. These techniques have led to application of modeling many different diseases. *Continuity*, a program for modeling and data analysis in bioengineering, is a powerful tool for finite element modeling in cardiac mechanics. It is available for download at <http://www.continuity.ucsd.edu/Continuity/Download>. Finite element models are a popular numerical technique used in modeling the heart. The mechanical and electrical properties of the heart can be modeled using partial derivative equations and the combination of elements and nodes are used to capture the complex

cardiac geometry. To properly define the heart structure, three dimensional hexahedral finite elements were used to model the geometry in prolate spheroidal coordinates (λ, μ, θ) . It has been shown in previous studies that this is an adequate realistic representation of the geometry [9, 18]. This coordinate system is advantageous as only the radial coordinate, λ , needs to be fitted to for our models to be an accurately capture the heart structure. MRI has become a powerful and non-invasive tool to perform cardiac imaging and can be used to create these realistic models. There are many available software programs, such as ITK-snap that can be used to perform manual segmentation of these images. Using *Continuity*, we can create an adequate representation of the heart geometry. However, the anatomical geometry is not sufficient for defining a complete cardiac model. There are other factors, such as the fiber architecture to consider. Diffusion tensor MRI (DT-MRI) has been shown to be a powerful tool to measure the fiber orientations of the heart [13]. Using *Continuity*, we can use the measured these measures values and define them in our models and now we can create a model that not only captures the anatomy but as well defines the fiber architecture.

For this project, we will use MRI images to quantify the end-diastolic structure of our normal and hypertensive rats to create the finite element models. The fiber architecture of the heart will be measured using diffusion tensor MRI (DT-MRI). Using *Continuity*, we will combine all this information to create an accurate model for both a hypertensive and normotensive heart.

1.4 Harmonic Phase Algorithm (HARP)

HARP is a powerful medical tool that is capable of extracting motion information in tagged MRI images. This technique was developed by Osman and Prince [1, 2, 3] and has begun to see widespread clinical use. The method uses band pass filters to isolate spectral peaks in the Fourier domain of the tagged images and calculates the phase images (HARP images) by taking the inverse Fourier transform of the isolated spectral peaks. Each material point has a unique phase that is invariant over time, and therefore HARP essentially tracks the motion of material points by following phase values over time.

We performed tagged MRI on our rat hearts and used HARP to track manually defined material points on the myocardium from end-diastole to end-systole. HARP has mostly only been used to track points on the LV wall [1, 2, 3, 18], however in this study, we show the power and accuracy of this tool to track the RV free wall as well. We combined these results and fit our finite element models to each frame to simulate the contraction of our rat hearts. Using this information, we calculated the three dimensional strain distributions.

1.5 Specific Aims

Specific Aim 1: To create 3D finite element models of the contracting heart for a control rat heart as well as a hypertensive rat heart. Develop upon existing techniques, such as HARP and DT-MRI post processing methods. The following techniques will be performed to accomplish this aim:

- Quantify the end-diastolic geometry and structure of normal and hypertensive rat hearts using FLASH-cine MRI scans to acquire the geometry of the in vivo heart at end diastole
- Use diffusion tensor imaging (DT-MRI) to find the cardiomyocyte (fiber) and myolaminar (sheet-normal) orientations.
- Using an improved version of HARP, track material points in the LV and RV and then the models are deformed to fit these points from end-diastole to end-systole.

Specific Aim 2: To measure deformation from end-diastole to end-systole of both the hypertensive and control model. We will specifically calculate circumferential, radial, longitudinal, fiber, sheet-normal, and cross-fiber strain distributions and compare to similar known results in rats and humans with hypertensive disease.

2 Materials and Methods

2.1 Animal Preparation

The experiments were performed on Dahl salt-sensitive rats (SS) purchased from Charles River. We separated ten rats into two groups, Control ($n = 5$), and Hypertensive ($n = 5$). The Control group was fed the same diet, AIN-76A (NaCl = 0.4%) until the age of twelve weeks. The hypertensive group was fed the low salt diet until the age of eight weeks, and then fed a high salt diet, AIN-76A (NaCl = 4.0%) for the remainder of time. At the age of twelve weeks, only two rats from each group were imaged using MRI to acquire *in-vivo* geometry of their hearts. Afterwards, hemodynamic measurements were

made to acquire ECG and pressure profiles for all the rats. Then, DT-MRI was only performed on two rats, one control and one hypertensive. We therefore only focused on performing our data analysis on these two rats. All protocols were performed according to the National Institutes of Health's (NIH) *Guide for the Care and Use of Laboratory Animals* and approved by the UCSD Animal Subjects Committee.

2.2 Hemodynamic Analysis

Pressure and ECG measurements were obtained with standard procedures used previously in the rat [8]. The rats were anesthetized initially with 5% (vol) inhaled isoflurane and maintained via a nose cone at 2% (vol), and kept at a constant body temperature with a circulating water blanket. The carotid artery was isolated and an excision was made to introduce a 1.8-Fr Mikro-Tip pressure catheter (SPR-839, Millar Instruments). This catheter advanced down the ascending aorta where the aortic pressure was then measured. The catheter was then moved into the LV cavity through the aortic valve where the LV pressure was recorded. Hemodynamic data were recorded and analyzed using DATAQ Instruments software. A total of five cardiac cycles were collected for each of the ten rats. Values found from the recordings for each animal (5-beat average) include end-diastolic and peak systolic pressure, heart rate, and mean arterial pressure.

2.3 Cardiac Magnetic Resonance Imaging

2.3.1 Anatomical and SPAMM Tagged cine MRI

The rats were imaged using a on a 7T horizontal-bore magnet (Varian, Palo Alto, CA, USA) with an Avance II console (Bruker, Germany). The gradient system of the scanner is capable of 100mT/m gradient strength and maximum ramp time of 210 μsec . The rats were scanned at twelve weeks of age.

The rats were first initially sedated with 5 vol-% isoflurane in 100% O₂ and then transferred to the bore magnet. They were continuously sedated with 1-2 vol-% isoflurane being delivered through a nose cone. ECG monitoring was performed with a control gating module (SA Instruments, Stony Brook, NY). The rat hearts were maintained at ~350 BPM. Using a regulated heated airflow, the bore temperature was maintained at ~37°C.

For the anatomical images, an ECG and respiratory triggered FLASH sequence was used with the following parameters: TE = 2.3 ms, TR = 9.45 ms, flip angle = 30°, 1.5 mm slice thickness, FOV = 6 x 5 cm, matrix size = 199 x 166, NR = 18. We first oriented the rat heart using localizer images and then proceeded to collect eight axial slices. We only collected the end diastolic frame for the anatomical images. We also collected one long axis slice that using the same parameters. Figure 2-1 shows the eight axial slices cropped to a region of interest around the left ventricle. For the tagging MRI, a Spatial Modulation of Magnetization (SPAMM) pulse sequence was used to modulate the anatomical images with a periodic pattern of stripes that deform with the heart wall. The tagging pulse consisted of two RF's pulses with a gradient in between and spoiler

gradient at the end. The tagging pulse was created using the following parameters: tag distance, 1.8 mm, tag thickness, 0.62 mm. Depending on the heart rate, 14-16 frames were collected. The parameters used for the anatomical images were the same for the tagged images. Figure 2-2 shows a single tagged axial slice over the time frames collected cropped to a region of interest around the left ventricle. The imaging protocol took approximately four hours for each rat.

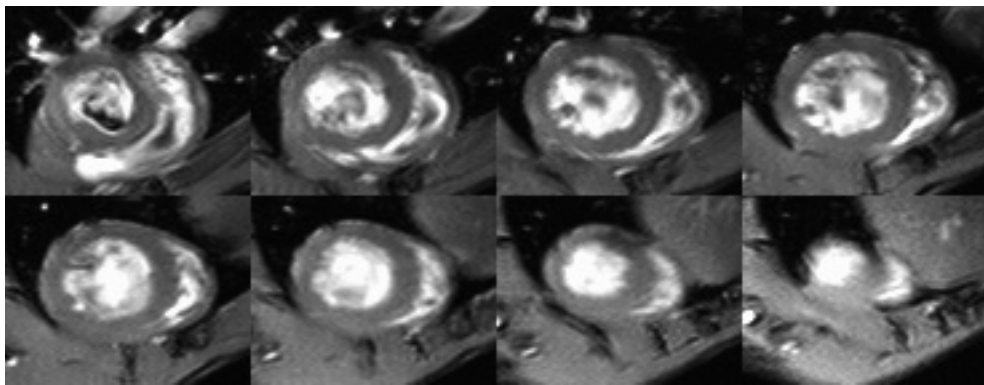


Figure 2-1: Example anatomical images taken from a single rat. Eight axial slices were collect from base(top left) to apex(bottom right).

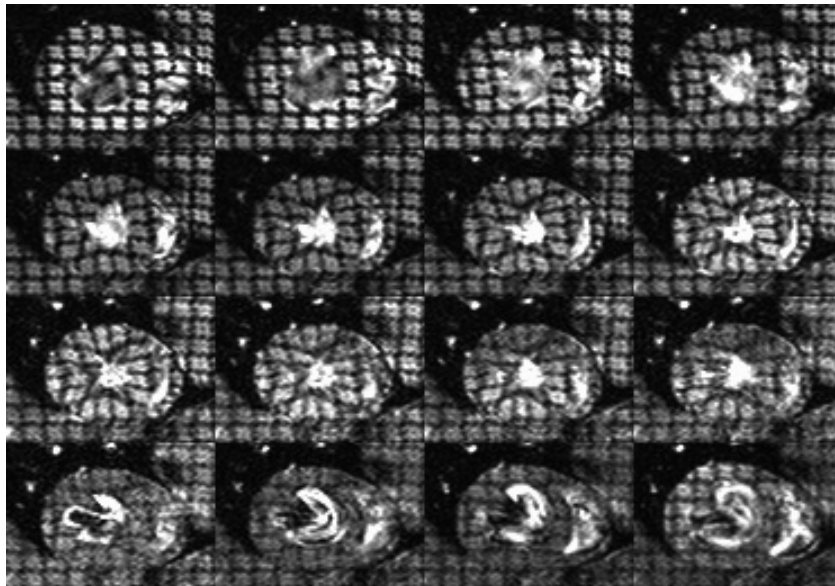


Figure 2-2: A sequence of tagged MRI of a rat heart. The images are sixteen time frames depicting the rat heart motion from end-diastole (top left) to end-systole(bottom right)

2.3.2 Diffusion Tensor MRI

After the SPAMM tagged images were collected, the rats were sacrificed and the hearts were excised. The hearts were then transferred to Florida and DT-MRI was performed using a 17T Bruker Biospan magnet using a standard DTI spin echo sequence. The following parameters were used in these experiments: TE = 23 ms, TR = 6000, B-value = $1000 \text{ s}\cdot\text{mm}^2$, twelve diffusion directions, FOV = 1.35 x 1.35 cm, matrix size = 224 x 224, slice thickness = 0.3 mm, NR = 4. Figure 2-3 is an example B0 image taken on one of the rats. We imaged fifty-five axial slices and total imaging protocol took 19 hours for each rat heart.

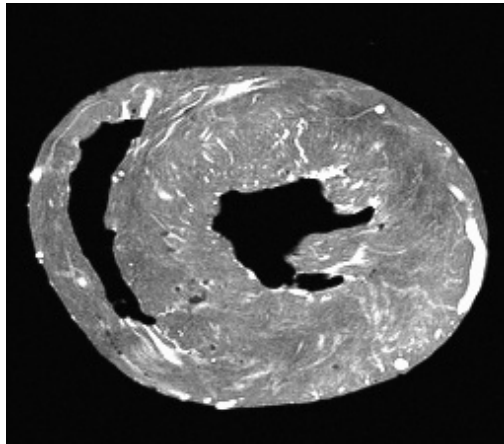


Figure 2-3: Example DT-MRI slice performed on a excised rat heart

2.4 Image Analysis

For the anatomical and SPAMM tagged images, a custom built code was built using MATLAB to convert the images to AFNI format. The images were interpolated to a matrix size of 256x256 using zero fill reconstruction. Data analysis was performed on the original and interpolated images to confirm this method produces the same results.

For each acquisition, the end-diastolic frame was chosen to be the image with the largest LV cavity and the end-systolic frame was the image with the smallest LV cavity. The LV epicardial and endocardial boundaries were extracted manually using ITK-SNAP software. These images were used as an input for the HARP algorithm and more detail will be presented in the next section. For the DT-MRI images, the data was converted to AFNI format using the code built from MATLAB and the AFNI software was utilized to analyze these images.

2.5 Harmonic Phase Algorithm (HARP)

There have been major developments in tagged cardiac imaging that have allowed fast strain calculation of the *in vivo* heart. MRI tagging involves using a special pulse to create vertical and horizontal lines called tags. Using FLASH-CINE sequences, we can show the motion of the heart as well as the tag features that displace with the heart. HARP analysis has become one of the most successful methods for measuring deformation of the heart using SPAMM tagged images. It involves tracking material points through the cardiac cycle and uses these results to calculate Lagrangian strain. Here we reproduce the HARP method employed by Osman et. al [1, 2] and Prince et. al [3] as well as perform some modifications in order to improve upon their method to achieve more accurate results. We will begin with a small background of SPAMM tagged images and then proceed to discuss the HARP algorithm.

The effect of tagging can be described as multiplication of the underlying image with a specific tagged pattern. This pattern can be written as a cosine series having a fundamental frequency that is specified by the tagging pulse. This pattern causes the

spectral peaks in Fourier space shown in figure 2-4. The tagging pulse determines the number of spectral peaks. A 1D SPAMM pattern generates $2N-1$ peaks where N is the number of RF pulses, but if a 2D pattern is used, than the number of peaks is $(2N - 1)^2$. The HARP method begins with using a band pass filter to isolate the spectral peaks of interest. We perform an inverse Fourier Transform and the result is a complex image with magnitude and phase, $\varphi(\mathbf{y}, t)$. The magnitude image is basically the underlying image, but blurred due to the filtering process. The key data is the phase, which gives information about the motion of the heart. The phase can be calculated by taking the inverse tangent of the imaginary part divided by the real part, however this is the “wrapped” value that only falls in the range $(-\pi, \pi)$, and not the true phase, $\varphi(\mathbf{y}, t)$. We denote the relationship between the true phase, $\varphi(\mathbf{y}, t)$, and the wrapped phase, $a(\mathbf{y}, t)$, by the following:

$$a(\mathbf{y}, t) = \mathcal{W}(\varphi(\mathbf{y}, t)) \quad [2-1]$$

where the non-linear wrapping function is given by

$$\mathcal{W}(\varphi) = \text{mod}(\varphi + \pi, 2\pi) - \pi \quad [2-2]$$

$a(\mathbf{y}, t)$ is denoted as the harmonic phase angle (HARP) image and can visualized with the magnitude image in figure 2-4. The underlying principle of HARP is that a material point retains its HARP angle throughout its motion; essentially the angle is material property of the tagged tissue [1, 2, 3]. In the next section, we will describe in detail the band pass filter selection process.

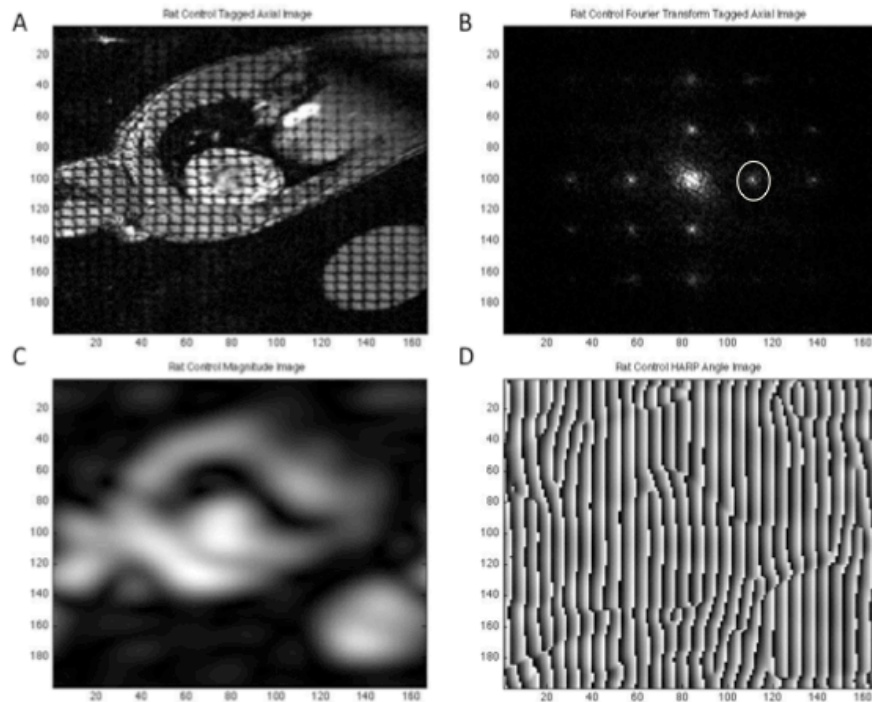


Figure 2-4: (A) Example of an axial tagged image from the control heart scans (B) Fourier transform of the tagged image (C) Magnitude image after isolating a spectral peak using a band pass filter (D) Phase image of the isolated spectral peak

2.5.1 Band pass Filter Selection

There have been many different types of band pass filters such as circular, elliptical, Gabor etc. Osman and Prince et al. [1, 2] used an elliptical filter for their calculations, however Denney Jr. et al. [4] has shown that the Gabor filters acquire more accurate results. In this study, each image produced different results when using the Gabor and elliptical filters, but no data suggested that one filter was superior to the other. Therefore, each slice was optimized to achieve the best results. The ellipse was chosen because it captures the shape of most spectral peaks [1, 2, 3]. This ellipse then tails off in a Gaussian fashion to reduce the ringing artifacts for points that lie outside the region. The Gabor filter is essentially a Gaussian modulated by complex sinusoidal [5].

If we let \mathbf{k} denote the 2-D frequency, then the elliptical filter used in the Fourier domain is shown below:

$$F(\mathbf{k}) = \begin{cases} 1 & s(\mathbf{k}) \leq 1 \\ e^{-\frac{(s(\mathbf{k})-1)^2}{2\sigma^2}} & s(\mathbf{k}) > 1 \end{cases} \quad [2-3]$$

where,

$$s(\mathbf{k}) = \|(RS)^{-1}(\mathbf{k} - H^T w)\| \quad [2-4]$$

In this equation, S is $\begin{bmatrix} Ra & 0 \\ 0 & Rb \end{bmatrix}$, where Ra and Rb are the major and minor radii of the elliptical region in mm^{-1} . H is $[h_1 \ h_2]$, where h_1 and h_2 are 2D orthogonal unit vectors that describe the image orientation. w is the location of the spectral peak of interest. R is a rotation matrix that rotates the ellipse so that major axis is parallel with the angle generated by $H^T w$. Figure 2-5 represents the filter used for these images. The radii have an enormous effect on the HARP tracking because if they are too small, than the accuracy will be poor, and if they are too big, than we introduce artifacts. In order to optimize the radii, we manually selected different values until the number of mis-tracked points was minimized.

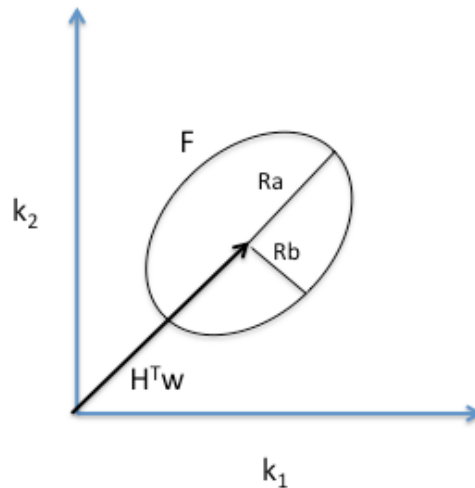


Figure 2-5: Example of the band pass filter centered at a frequency w

The Gabor filter used for these studies was taken from Denney Jr. et al [4] and it can be described by the following equation:

$$H(\mathbf{k}) = \frac{1}{4\pi\sigma_x\sigma_y} \left[e^{-\frac{1}{2}(\mathbf{k}-\mathbf{w}_T)^T \mathbf{B}^{-1}(\mathbf{k}-\mathbf{w}_T)} + e^{-\frac{1}{2}(\mathbf{k}-\mathbf{w}_T)^T \mathbf{B}^{-1}(\mathbf{k}-\mathbf{w}_T)} \right] \quad [2-5]$$

where,

$$\mathbf{B} = \begin{bmatrix} \sigma_x^2 & 0 \\ 0 & \sigma_y^2 \end{bmatrix}, \mathbf{w}_T = \begin{bmatrix} \frac{1}{T} \\ 0 \end{bmatrix} \quad [2-6]$$

σ_x^2 and σ_y^2 are frequency-domain variances and T is the tag spacing. σ_x^2 and σ_y^2 were optimized for each slice. Now that we have our band pass filters, we can isolate the spectral peaks of interest. We select two peaks where one gives information about the

vertical motion (I_v) and the other gives information about the horizontal motion (I_h). We can then calculate the HARP images, which results in $a_h(\mathbf{y}, t)$ and $a_v(\mathbf{y}, t)$.

2.5.2 HARP Tracking Algorithm

Because the phase, $\varphi(\mathbf{y}, t)$, cannot be directly calculated, we use the HARP angle in our computations. Because the phase value is “wrapped”, there exists no unique phase angle for each point. For a given material point, only one of these points can be a correct match. If the motion is small from one image to the next, then the point with same pair of HARP angles will be close to the original point. We now formally develop this approach. Consider a material point \mathbf{y}_m at a time, t_m . If the point moves to \mathbf{y}_{m+1} at a time, t_{m+1} , then the phase at this point must be equal to the phase of the original point.

$$\varphi(\mathbf{y}_{m+1}, t_{m+1}) = \varphi(\mathbf{y}_m, t_m) \quad [2-7]$$

This equation is the basis for tracking a point, \mathbf{y}_m , from time t_m to t_{m+1} . The goal is find \mathbf{y} that satisfies the following equation:

$$\varphi(\mathbf{y}_{m+1}, t_{m+1}) - \varphi(\mathbf{y}_m, t_m) = 0 \quad [2-8]$$

In order to find a solution to this equation, we use the Newton-Rhapson technique. The equation is shown below:

$$\mathbf{y}^{(n+1)} = \mathbf{y}^{(n)} - [\nabla\varphi(\mathbf{y}^{(n)}, t_{m+1})]^{-1} [\varphi(\mathbf{y}^{(n)}, t_{m+1}) - \varphi(\mathbf{y}_m, t_m)] \quad [2-9]$$

where ∇ is the gradient with respect to \mathbf{y} .

There are several modifications that need to be done to this equation because $\varphi(\mathbf{y}, t)$ is not calculated, and $a(\mathbf{y}, t)$ is used instead. We say that the gradient of $a(\mathbf{y}, t)$ is the same as $\varphi(\mathbf{y}, t)$ except at the wrapping artifact, where the gradient magnitude tends to be very large. However, if we add π to $a(\mathbf{y}, t)$ and rewrap this value, the gradient of this result will be equal to $\varphi(\mathbf{y}, t)$ wherever the wrap occurred. Formally, we can write this as the following:

$$\nabla\varphi = \nabla * \mathbf{a} \quad [2-10]$$

where,

$$\mathbf{a} = \begin{bmatrix} a_h \\ a_v \end{bmatrix} \text{ and } \nabla * \mathbf{a} = \begin{bmatrix} \nabla * a_h \\ \nabla * a_v \end{bmatrix} \quad [2-11]$$

and,

$$\nabla * a_k = \begin{cases} \nabla a_k \\ \nabla \mathcal{W}(a_k + \pi) \end{cases} \quad \|\nabla a_k\| \leq \|\nabla \mathcal{W}(a_k + \pi)\|, k = h, v \quad [2-12]$$

The second problem of using this equation is the difference, $\varphi(\mathbf{y}^{(n)}, t_{m+1}) - \varphi(\mathbf{y}_m, t_m)$, which we cannot calculate because we do not know the true phase values.

However, if we assume that $\|\varphi(\mathbf{y}^{(n)}, t_{m+1}) - \varphi(\mathbf{y}_m, t_m)\| < \pi$, a small motion assumption, then the following must hold true.

$$\varphi(\mathbf{y}^{(n)}, t_{m+1}) - \varphi(\mathbf{y}_m, t_m) = \mathcal{W}\left(\mathbf{a}(\mathbf{y}^{(n)}, t_{m+1}) - \mathbf{a}(\mathbf{y}_m, t_m)\right) \quad [2-13]$$

Thus our final equation becomes the following:

$$\mathbf{y}^{(n+1)} = \mathbf{y}^{(n)} - [\nabla * \mathbf{a}(\mathbf{y}^{(n)}, t_{m+1})]^{-1} \left[\mathcal{W}\left(\mathbf{a}(\mathbf{y}^{(n)}, t_{m+1}) - \mathbf{a}(\mathbf{y}_m, t_m)\right) \right] \quad [2-14]$$

There are several problems to consider in the use of this equation. As stated before, because of the phase wrapping, the solution is not unique, there will be many points that can satisfy this solution, therefore it is necessary to start with a good initial point and to restrict the step size to prevent jumping to the wrong solution. Thus we limit our step size to one pixel and initialize our starting point, $\mathbf{y}^{(0)} = \mathbf{y}_m$. We also must be able to calculate $\mathbf{a}(\mathbf{y}, t_{m+1})$ for an arbitrary \mathbf{y} . Normally, we could use straight bilinear interpolation, however this tends to produce poor results due to the wrapping artifacts [1, 2, 3]. Therefore, we do a local phase unwrapping of \mathbf{a} around the point \mathbf{y} , then perform bilinear interpolation of the unwrapped angle and the wrap the result to give us an interpolated HARP angle [1, 2, 3]. The stop criterion used for this algorithm is when either the angles are close to the original HARP vector or when the maximum iteration number is exceeded.

We can now summarize this algorithm for the tracking of one point from one image to another. We consider \mathbf{y}_{init} to be our starting point and \mathbf{a}^* to be our desired HARP vector. We set $\mathbf{y}_m = \mathbf{y}_{init}$, and $\mathbf{a}^* = \mathbf{a}(\mathbf{y}_m, t_m)$, pick a maximum iteration number, N .

Algorithm 1, let $n = 0$ and set $\mathbf{y}^{(0)} = \mathbf{y}_{init}$,

- 1) If $n > N$ or $\|\mathcal{W}(\mathbf{a}(\mathbf{y}^{(n)}, t_{m+1}) - \mathbf{a}^*)\| < \varepsilon$, then the algorithm terminates with

$$\mathbf{y}_{new} = \mathbf{y}^{(n)}$$

- 2) Compute a step direction, \mathbf{v}

$$\mathbf{v}^{(n)} = -[\nabla * \mathbf{a}(\mathbf{y}^{(n)}, t)]^{-1}[\mathcal{W}(\mathbf{a}(\mathbf{y}^{(n)}, t) - \mathbf{a}^*)]$$

- 3) Compute a step size

$$\alpha^{(n)} = \min\left\{\frac{1}{\|\mathbf{v}^{(n)}\|}, 1\right\}$$

- 4) Update the new point

$$\mathbf{y}^{(n+1)} = \mathbf{y}^{(n)} + \alpha^{(n)}\mathbf{v}^{(n)}$$

- 5) Increment n and go to step 1

For our calculations, we used a maximum of iterations of twenty-five ($N = 25$) and $\varepsilon = 0.01$. In order to track a point through a series of images, we simply apply this algorithm to each image in the sequence. At t_{m+2} , the initialization use is \mathbf{y}_{new+1} , the estimated position from the previous frame. The target HARP vector on the other hand remains the same throughout the entire sequence. This algorithm finds points with the same HARP angles and attempts to avoid jumping to the wrong solution by limiting the

step size and keeping the initial point close to desired solution. Therefore, if we wanted to apply this method for multiple frames, we perform the following.

Algorithm 2, set $\mathbf{a}^* = \mathbf{a}(\mathbf{y}_m, t_m)$, $\hat{\mathbf{y}}_m = \mathbf{y}_m$, and $i = m$.

- 1) Set $\mathbf{y}_{init} = \hat{\mathbf{y}}_i$
- 2) Apply Algorithm 1 with t_{i+1} , to yield \mathbf{y}_{new}
- 3) $\hat{\mathbf{y}}_{i+1} = \mathbf{y}_{new}$
- 4) Increment i and go to step 1

This algorithm has been shown to produce highly accurate results [1, 2, 3], however, this method still produces mis-tracked points. These errors occur when points move through the plane and phase values become lost or when motion is too large and the HARP small motion assumption is violated. Because of the HARP standard tracking approach, the tracking will converge to the incorrect points during the lost frames and generally will not find the correct points when it reappears in the later frames. Normally, one can remove these points manually, however this can be very time consuming for many points, therefore it is very important to improve the accuracy of the HARP tracking. In order to improve the quality of the tracking, Prince et al. [4] defined a new method that improves upon this traditional tracking method, which we call *shortest path HARP refinement* (SP-HARP). Standard HARP tracking methods solely considers the temporal dependency of a point trajectory, whereas SP-HARP considers the spatial component for each point. Essentially this method improves the initial guess for each point so that the material point will be tracked correctly.

2.5.3 Short Path HARP Refinement (SP-HARP)

We first begin by defining a seed voxel, which is assumed to be correctly tracked using the standard HARP method. SP-HR tracks all the pixels in the image by using a region-growing algorithm. In order to prevent all the points in one image from being tracked, we create a mask so that only the points of interest are tracked. In SP-HR, the optimal path is calculated from each point in the image to the seed voxel.

The image is represented as an undirected graph, $G = (V, E)$ where V is the set of vertices, and E is the set of edges. If we consider tracking points at a time t_1 to a later time frame t_2 , each pixel $\mathbf{y}(t_1)$ in the image is represented as a vertex v in the graph. Each edge, $e_{ij} = \langle v_i, v_j \rangle$ in E corresponds to neighboring vertices, v_i and v_j . We compute edge cost, $C_E(e_{ij})$, which is a non-negative number that measures the dissimilarity between a neighboring vertex pair. Also, each vertex has a corresponding vertex cost, $C_V(v)$, which is essentially the sum of the edge costs of from the seed vertex to the vertex v along the optimal path. Both types of cost will be discussed in more detail below.

2.5.3.1 Cost Functions

We define the edge cost using the implied motion of a vertex from one frame to a later frame. Since the motion is smooth, the displacements of neighboring points should be similar. Formally, we say if $y_i(t_1)$ and $y_j(t_1)$ are adjacent points at time t_1 , and at time t_2 , they move to $y_i(t_2)$ and $y_j(t_2)$, the differences between their displacements should be small. If we assume $y_i(t_1)$ is correctly tracked to $y_i(t_2)$, then we can find the approximate displacement for $y_j(t_1)$ to $y_j(t_2)$. We define the following:

$$y'_j(t_2) = y_j(t_1) + y_i(t_2) - y_i(t_1) \quad [2-14]$$

$y'_j(t_2)$ should be approximately equal to $y_j(t_2)$ and if this is true, then both their harmonic phase values should be approximately equal and the difference between the original phase at t_1 and the new phase at t_2 should be small. We define this quantity as the following:

$$\Delta(y_i, y_j) = \sum_{k=1}^2 \left\| \mathcal{W} \left(a_k(y_j(t_1), t_1) - a_k(y'_j(t_2), t_2) \right) \right\| \quad [2-14]$$

Finally, we define the edge cost function associated between two neighboring points y_i and y_j :

$$C_E(e_{ij}) = \Delta(y_i, y_j) \quad [2-15]$$

Given a seed vertex, v_0 , we define the vertex cost function $C_V(v_i)$ at any other vertex v_i as the sum of the edge costs along the shortest path from v_0 to v_i . For any path $p = \langle v_0, v_1, v_2, v_3 \dots v_i \rangle$, its accumulated cost is the following:

$$C(p) = \sum_{k=1}^i C_E(\langle v_{k-1}, v_k \rangle) \quad [2-16]$$

Therefore the vertex cost function at v_i is

$$C(v_i) = \min\{C(p): p \text{ is any path from } v_0 \text{ to } v_i\} \quad [2-17]$$

$C(v_0)$ is set initially to be zero. The vertex cost function is used to find the optimal path from the seed vertex to any other vertex. Knowing the path, we can find the initial displacement for the vertex of interest and then we can use this new initial starting point and the standard HARP tracking method to track the vertex of interest to a later frame.

2.5.3.2 Motion Tracking via SP-HARP

In SP-HR, the shortest path from the seed vertex to every other point is solved using Dijkstra's algorithm. Overall, the algorithm is a region-growing algorithm in the sense that boundary pixels are successively added to the growing list of points comprising a region. The boundary points however must lie in the user defined mask such that the whole image is not tracked but only the points of interested. In addition to keeping track of the region itself, we also must keep track of the predecessor of the vertex of interest along the shortest path. When a new point is added on the basis that its vertex cost is the smallest, it is tracked using the standard HARP tracking method, but the point is initialized using the displacement of the point's predecessor along the shortest path.

In order to carry out Dijkstra's algorithm, we classify the vertices into three distinct sets: the boundary vertex set V_b , the tracked vertex set V_t , and the unvisited

vertex set V_u . We denote $N(v)$ to be the predecessor of v along its shortest path, and $u(v)$ to be the displacement associated with v . With all these parameters defined, we summarize the SP-HR algorithm as the following:

1. Manually pick a seed vertex, v_0 . Set $N(v) = v_0$, and $u(v_0) = 0$. Initialize $V_t = 0$, $V_b = \{v_0\}$, and $V_u = V \setminus \{v_0\}$. Set $C_V(v_0) = 0$, $C_V(v) = \infty$, for $\forall v \in V_u$.
2. Find the vertex v_k with the smallest C_V in list V_b . Find the shortest path from v_0 to v_k , find $N(v_k)$. Set the displacement to be $u(N(v_k))$. Track the point y_k associated with v_k using the traditional HARP method, but using the initialization of $y'_k = y_k(t_1) + u(N(v_k))$. Set $V_t = V_t \cup \{v_k\}$.
3. For each v_i such that $\langle v_i, v_k \rangle \in E$ and $V_t \not\ni v_i$ and v_i lies in the user defined mask. Compute the edge cost $C_E(e_{ij})$ and update the vertex cost function $C_V(v_i)$
 - a. Compute the new cost $C_V'(v_i) = C_V(v_k) + C_E(e_{ki})$
 - b. If it is larger than the existing cost, i.e., $C_V'(v_i) > C_V(v_i)$, do nothing
 - c. Otherwise, set $C_V'(v_i) = C_V(v_i)$, and $N(v_i) = v_k$. Set $V_b = V_b \cup \{v_i\}$ and $V_u = V_u \setminus \{v_i\}$.
4. If $V_b \neq 0$, go to Step 2. Otherwise exit the algorithm

The SP-HR algorithm described only tracks points from t_1 to t_2 . In order to track through a series of frames, we use this method for each frame and update the seed voxel each frame. The algorithm is described below:

1. We manually define the seed voxel, y_0 for the frame t_i and track this point throughout all the frames using standard HARP tracking

2. We perform SP-HR to track points from t_i to t_{i+1}
3. We increment i and update the seed voxel, y_0 for the next frame. Go to Step 2 until all frames have been processed

The SP-HARP method did show improvement especially for the material points that have large deformation. Even with this improvement, there are still many errors generated that cause the strain calculations to be very noisy. In order to eliminate the noise, we employed a smoothing technique on the deformations maps to correct the mistracked points. Prince et al. [6] used anisotropic diffusion smoothing on the components of the gradients of the displacement in order to improve the strain calculations. This strategy aims at a target somewhat at the midpoint between the raw data and the final strain map, and it is also immune to phase wrapping [6]. Prince et al. [6] used the magnitude images from the HARP images as a mask so that the points along the mask would only be smoothed. Here, we manually create a mask and smooth the gradient displacement images for each frame to correct the poorly tracked points. Using this technique we can now track the material points with extremely high accuracy.

2.6 Cardiovascular Model

The cardiovascular model used is very similar to that used in McCulloch et al. [9]. The anatomical model consists of the geometry obtained from the end-diastolic anatomical MRI images and the fiber-sheet orientations. The bi-ventricular geometry is modeled as a 3D hexahedral cubic-Hermite finite-element mesh (128 elements, 209 nodes) [9]. In order to determine the fiber architecture, we must first calculate the diffusion tensor from the DT-MRI. However these images represent the excised heart and

do not correspond to end-diastolic geometry. Therefore to find the correct fiber-sheet orientation, we must warp the fiber architecture results of the excised heart geometry to the end-diastolic geometry. AFNI software was utilized to calculate the diffusion tensor for the DT-MRI images and this data was filtered to remove noise using custom-built MATLAB code. The fiber architecture was represented by a local myofiber-sheet material coordinate system calculated from the eigenvectors of the diffusion tensors interpolated in Log-Euclidean space [9]. We created a bi-ventricular model for the excised heart geometry that was composed of a cubic-Hermite finite-element mesh (512 elements, 762 nodes). These results were registered to the corresponding ventricular geometry and the diffusion tensor was calculated for each node [9]. By calculating the deformation gradient between the two models, we can transform fiber architecture of the excised heart to the end diastolic geometry.

2.6.1 Anatomical Model

2.6.1.1 Bi-ventricular Geometry

The hexahedral cubic-Hermite finite element meshes of the ventricular geometries were constructed from the anatomical MRI and DT-MRI images. The epicardial and endocardial boundaries were manually segmented using ITK-SNAP for both the excised and end-diastolic heart geometries. An initial 2D mesh (129 nodes, 108 elements) consisting of four surfaces representing the epicardial and endocardial boundaries defined in prolate spheroidal coordinates. The model was then fitted to the surfaces that were segmented using the MRI images. Detailed description of the procedure can found in McCulloch et al. [9]. The fitted surfaces were converted to hexahedral cubic-Hermite

elements in rectangular Cartesian coordinates. The end-diastolic and excised models were refined to a final resolution of 209 nodes and 128 elements and 762 nodes and 512 elements respectively.

2.6.1.2 Ventricular Fiber Architecture

Basser et al. [13] stated that DT-MRI could be used to find the anatomical fiber directions for a heart by decomposing the diffusion tensor matrix into its eigenvalues and eigenvectors. The principal, secondary, tertiary eigenvector corresponds to fiber, cross-fiber, and sheet-normal direction respectively [43]. Using this information, it is therefore possible to reconstruct the architecture in the bi-ventricular models with a local orthogonal coordinate system calculated from the eigenvectors of interpolated diffusion tensors.

The first step was to calculate the diffusion tensors of our image using the AFNI software. Using custom built MATLAB code, noisy data was filtered based on unreasonable fractional anisotropy (FA) values or negative eigenvalues. The diffusion tensor images were segmented by the technique described previously. The images were then registered to the anatomical model by calculated a transformation matrix, \mathbf{T} , that rotates and translate the segmented images [9]. Since we rotated the coordinates, the tensors must also be rotated. A rotated tensor can be calculated by computing the rotational component, \mathbf{R} , of the transformation matrix and apply it to the diffusion tensor [9]. Figure 2-6 represents the results of using this technique. The fitting procedure was identical to McCulloch et al. [9], where the diffusion tensor was transformed into the Log-Euclidian space, $L = \log(D)$, and the individual components were fitted by the

same method as the anatomical models.

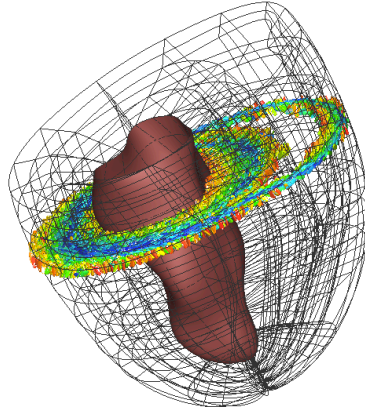


Figure 2-6: An example of the fitted anatomical model with a aligned reconstructed slice from the DT-MRI images before fitting. The slices were aligned with the model and the tensors were rotated as well.

2.6.1.3 Mapping the Fiber Architecture to the End-Diastolic Models

In order to compute the correct fiber architecture for the end-diastolic models, we must compute a deformation gradient matrix, \mathbf{F} , which can accurately rotate and translate the diffusion tensors to the target models (End-diastolic models). The smoothness of \mathbf{F} can be measured in term of its harmonic energy [9,14], which is defined as the squared Frobenius norm of the Jacobian of \mathbf{F} . Using the techniques in McCulloch et al. [9], we can calculate \mathbf{F} between the end-diastolic model and the excised model at the locations of the previously registered DT-MRI measurements. We then rotate the diffusion tensors using \mathbf{F} and the individual components of the tensor were fitted using the same manner as the excised heart model (see Figure 2-7).

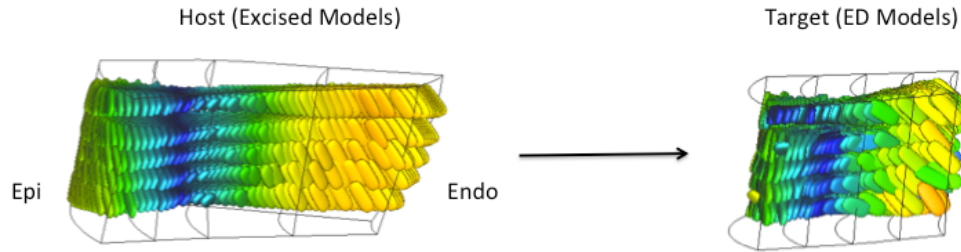


Figure 2-7: A view of the transformation used to reorient the diffusion tensors. The interpolated fibers are shown in four elements in the LV wall. The fiber architecture was reoriented by calculating \mathbf{F} between the material points in the excised and the end-diastolic models.

2.6.2 Lagrangian Strain Analysis

In order to calculate 3D Lagrangian strain distributions, the models were deformed to fit the HARP material points from end-diastole to end-systole. The end-diastolic frame was set as the undeformed reference state. The deformation modeling was done similar to McCulloch et al. [9]. The pre-fitted meshes were fitted in the radial, λ , coordinate to the raw data using a linear squares method [9]. Each frame was fitted using this approach to deform the models. In order to account for the lack of longitudinal information due to only collecting one long axis scan, we measured the shortening percentage in the long axis direction and assumed the focus value changed by the same number. Once we collected the fitted deformed models, we calculated the deformation tensor, \mathbf{F} , between two frames and then the lagrangian strain can be calculated using the following equation [18]:

$$\mathbf{E} = \frac{1}{2}(\mathbf{F}^T \mathbf{F} - \mathbf{I}) \quad [2-18]$$

2.6.3 Preliminary Ventricular Simulations

These models are useful in order to produce accurate strain distributions but the future objective is to simulate ventricular contraction and validate the results using these measured strain distributions and hemodynamics. Here, we present preliminary simulation results using a model similar to McCulloch et al. [9]. The cardiovascular model is composed four main components. The first component is the previously described anatomical model. The second component of the cardiovascular model is the constitutive law [10] for the passive material properties of the myocardium. The third component is the active-contractile model that simulates muscle contraction [11]. The parameters of this model were adjusted to match the hemodynamics in the rats. The fourth component consists of the lumped-parameter hemodynamic model [12] that is used as the load for the ventricular finite element model. We created a model for both the control rat and the hypertensive rat.

2.6.3.1 Passive Material Properties

For our simulations, we need to properly model the resting properties of the myocardium. We make use of the constitutive model developed by Odgen and Holzapfel [10]. In this model, the anisotropy in the fiber and cross-fiber directions are modeled by using different exponential terms. The following equation represents the strain energy function:

$$\psi = \frac{a}{2b} \exp[b(I_1 - 3)] + \sum_{i=f,s} \frac{a_i}{2b_i} \{ \exp[b_i(I_{4i} - 1)^2] - 1 \} \quad [2-19]$$

$$+ \frac{a_{fs}}{2b_{fs}} [\exp(b_{fs}I_{8fs}^2) - 1]$$

I_1 corresponds to the first invariant of the right Cauchy-Green strain tensor, I_{4f} and I_{4s} corresponds to the components of the right Cauchy-Greens strain tensor in the fiber and sheet direction respectively, and I_{8fs} corresponds to the coupling invariant. For our simulations, we set the constants, a_{fs} and a_s to zero. The parameters used for the other material constants, a_f , a , b , and b_s can found in Odgen and Holzapfel [10]. It is important to note that these parameters were not optimized for the rat models and human parameters were used.

To perform the contraction simulations, it is necessary to find the unloaded geometry for our rat models. We followed the procedure listed in McCulloch et. al [9], where they showed that the unloaded geometry can be found by estimating the unloaded state and inflating it to the end-diastolic pressure. They iterated this process until the loaded geometry was matched within measurement accuracy to the end diastolic geometry [9].

2.6.3.2 Active Contraction Model and Hemodynamic Model

Once we obtained the unloaded geometry and the passive material parameters, we used the active contraction model presented by Arts et al. [11], and adjusted the parameters until the pressure simulations matched the measured hemodynamics.

For the hemodynamics model, we chose to use the three-element arterial

windkessel model. This model contains three main elements, arterial compliance, C , aortic impedance, Z , and the total peripheral resistance, R (see Figure 2-8).

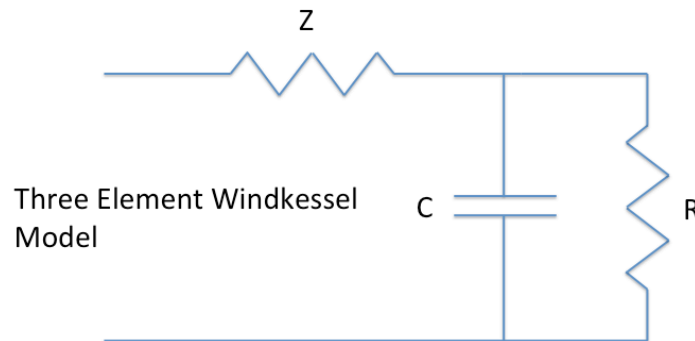


Figure 2-8: A representation of the three-element windkessel model. Z represents the aortic impedance, C represents the arterial compliance, and R represents the total peripheral resistance

In order to optimize these parameters, we first must measure the time constant τ , which is equal to $\frac{1}{RC}$. For the two-element windkessel model, the diastolic pressure, $P_{dia}(t)$, will decay by the following exponential [12]:

$$P_{dia}(t) = P_{es} e^{-\frac{t}{RC}} \quad [2-20]$$

where,

$$P_{es} = \text{end} - \text{systolic aortic pressure}$$

We can use this information to find the time constant, where the P_{es} is set as the pressure following the dicrotic notch [12]. Using this information, we performed exponential fits (see Figure 2-9) on the measured aortic pressure curves for five beats and averaged the

time constants. With the time constant value, we manually adjusted the R and C constants until the simulated aortic and LV pressure curve matched the measured hemodynamics. Z was approximated to be between 5%-7% of R . The algorithm runs from end-diastole to end-systole as the refilling stage cannot be simulated with this hemodynamic model.

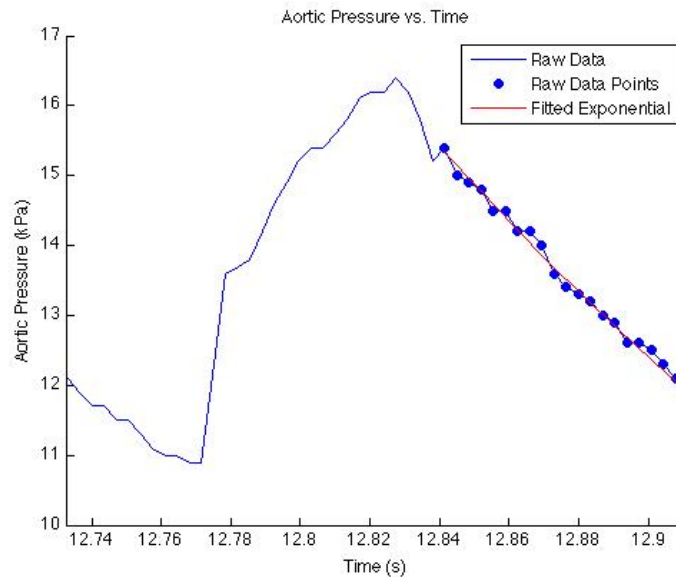


Figure 2-9: Example exponential fitting on the aortic pressure curve. The end systolic pressure was set as the following pressure point after the dicrotic notch.

3 Results

3.1 Rat Anatomical Model

The DT-MRI measurements were fitted to the excised models for both the control and hypertensive heart. The fiber architecture was calculated from the eigenvectors of the interpolated diffusion tensor. Figure 3-1 represents the raw DT measurements and fitted data for both the control and hypertensive models respectively.

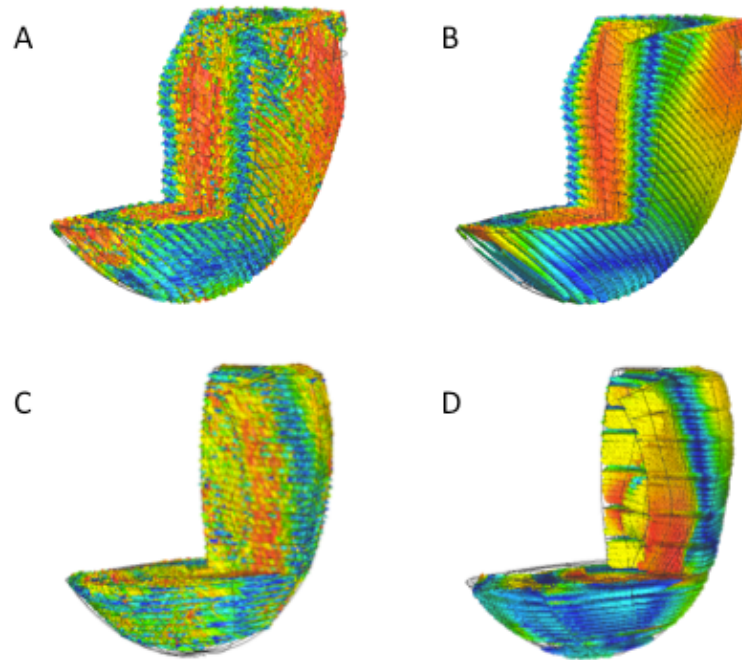


Figure 3-1: (A) Raw DT measurements for the control model (B) Fitted results for the control model (C) Raw DT measurements for the hypertensive model (D) Fitted results for the hypertensive model

In order to evaluate the quality of the fit, tensor error metrics were computed between the raw and fitted data [9, 14]. Let D be the diffusion tensor for the raw data. We let $\lambda_1, \lambda_2, \lambda_3$ be its eigenvalues in descending order with the corresponding eigenvectors e_1, e_2, e_3 .

Similarly, we denote D' the diffusion tensor for the fitted data with the corresponding eigenvalues, $\lambda_1', \lambda_2', \lambda_3'$, and eigenvectors, e_1', e_2', e_3' . Many different tensor metrics may be calculating, but the most relevant error metric is the overlap between e_i' and e_i

(See equation shown below)

$$C_t = \frac{\sum_{i=1}^3 \lambda_i \lambda_i' (e_i \cdot e_i')^2}{\sum_{i=1}^3 \lambda_i \lambda_i'} \quad [3-1]$$

The overlap equations states that C_i ranges between zero and one, where zero indicates no overlap and one indicates complete overlap. A histogram of the overlap error is shown in Figure 3-2 for both the control and hypertensive model respectively. Linear interpolation of the diffusion tensor components registered 216,210 of 318,067 DT measurements (67.98%) with an overlap greater then 0.7 for the control model. The hypertensive model registered 222,461 of 312,446 DT measurements (71.20%) with an overlap greater then 0.7. For both models, the highest area of agreement occurred in LV free wall (see Figure 3-3). The areas with poor overlap occurred in the right ventricle where the DT measurements contained noisier and more unreliable data (see Figure 3-4).

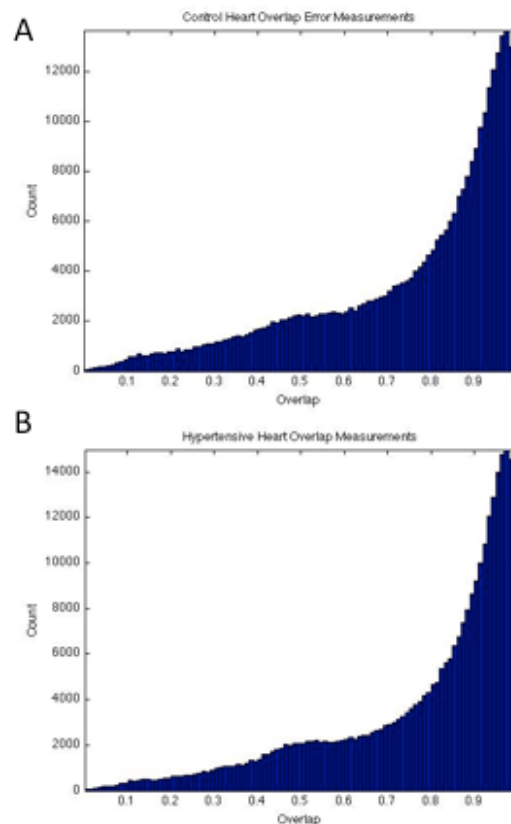


Figure 3-2: (A) Histogram of the overlap measurement for the control model. (B) Histogram of the overlap measurement for the hypertensive model.

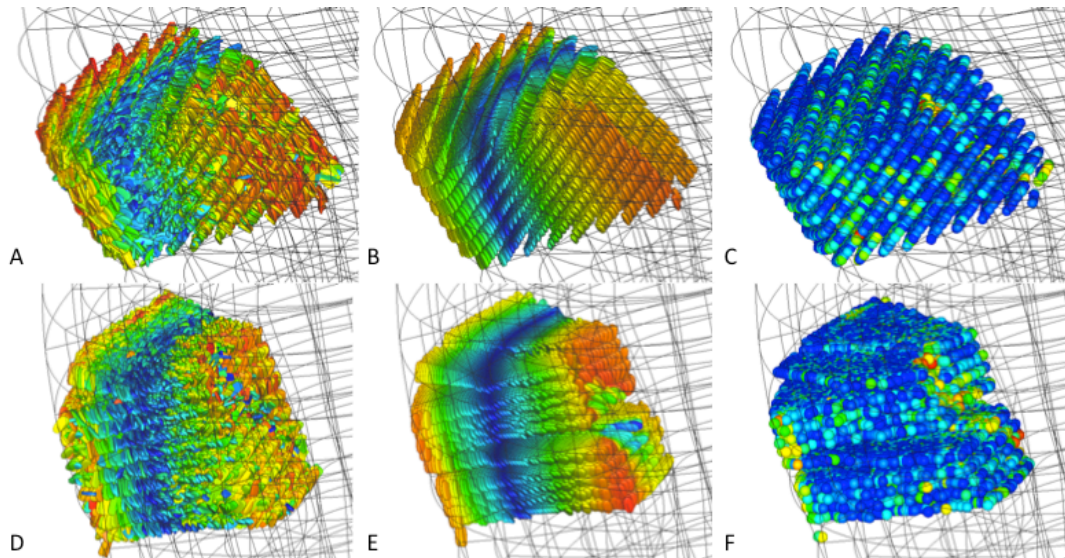


Figure 3-3: (A) Raw diffusion tensor data in four elements across the LV lateral wall for the control model. (B) Interpolated diffusion tensor data in four elements from the fit of the DT individual components for the control model. (C) The overlap error measurement between (A) and (B), blue corresponds to high overlap, red, corresponds to low overlap (D) Raw diffusion tensor data in four elements across the LV lateral wall for the hypertensive model. (E) Interpolated diffusion tensor data in four elements from the fit of the DT individual components for the hypertensive model. (F) The overlap error measurement between (D) and (E), blue corresponds to high overlap, red, corresponds to low overlap

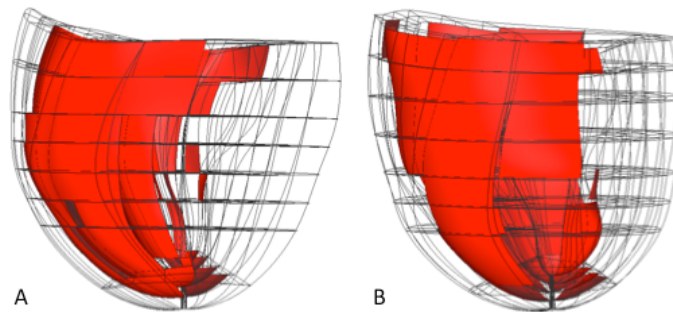


Figure 3-4: (A) and (B) Regions of poor overlap (marked in red) for both the control and hypertensive models respectively

The deformation gradient, \mathbf{F} , was calculated between the excised and end-diastolic geometries for the control and hypertensive models. We applied this gradient to the fitted diffusion tensor results to determine the fiber architecture for the ED models. The individual components of the rotated diffusion are then fitted in the same manner as the

excised models. Figure 3-5 represents the rotated DT measurements and fitted data for both the control and hypertensive models respectively.

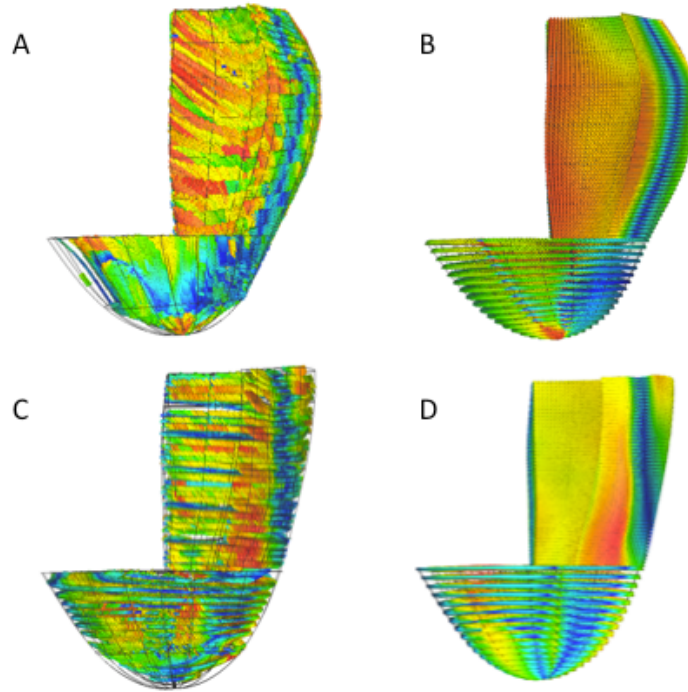


Figure 3-5: The deformation gradient was calculated between the excised and ED models and this gradient was applied to the fibers in order to find the architecture of the ED models(A) Raw DT measurements for the control model (B) Fitted results for the control model (C) Raw DT measurements for the hypertensive model (D) Fitted results for the hypertensive model

3.2 HARP Tracking

The tracking algorithm described previously was applied to the SPAMM tagged images collected from the control and hypertensive heart. Masks were manually created using AFNI, and since HARP is not limited to the resolution of the image, we interpolated points and a total between 5,000-9,000 points were tracked. Figure 3-6 and 3-7 represents the entire sequence of deformed states for a single axial slice from end-diastole to end-systole for the control heart and hypertensive heart respectively. We also applied the tracking algorithm to the long axis slices for both the control and hypertensive

heart. Figure 3-8 and 3-9 represents the entire sequence of deformed states for a single long axis slice from end-diastole to end-systole for the control heart and hypertensive heart respectively. Around 10% of the points were mis-tracked and these were either smoothed out using the previously described technique or removed manually. The locations of the mis-tracked points were mostly located near the edges of the myocardium. Using these deformation maps, we can now deform our models to fit these points.

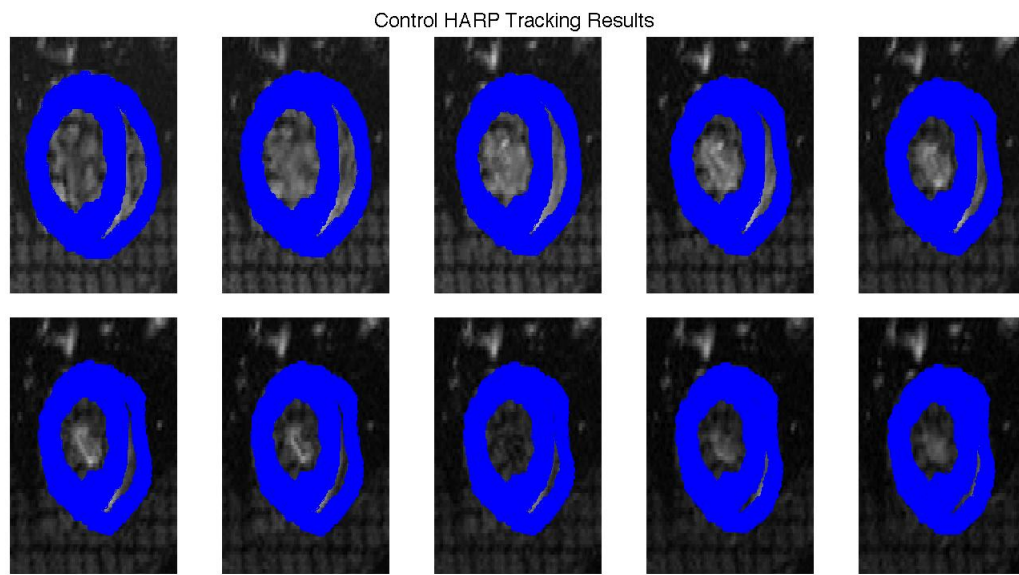


Figure 3-6: HARP tracking results for a control heart axial slice. The top left represents the end-diastolic frame, while the bottom right is the end-systolic frame.

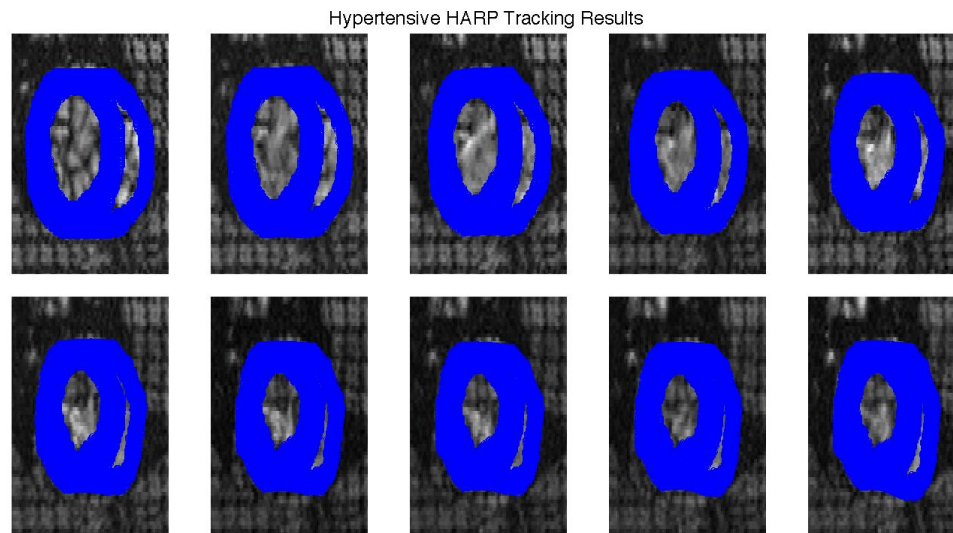


Figure 3-7: HARP tracking results for a hypertensive heart axial slice. The top left represents the end-diastolic frame, while the bottom right is the end-systolic frame.

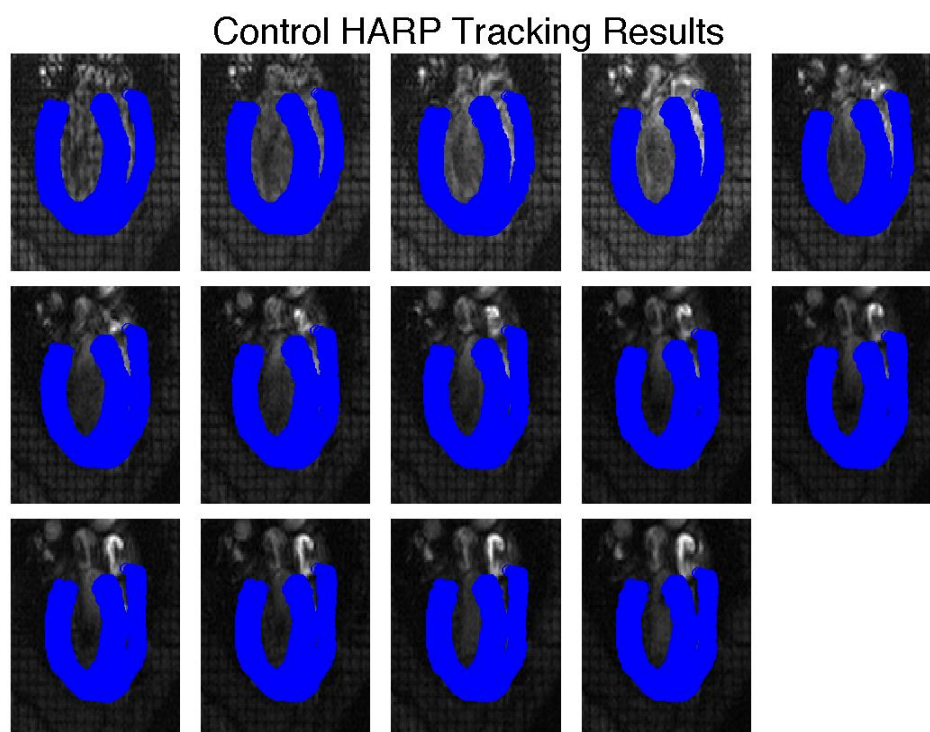


Figure 3-8: HARP tracking results for a control heart long axis slice. The top left represents the end-diastolic frame, while the bottom right is the end-systolic frame.

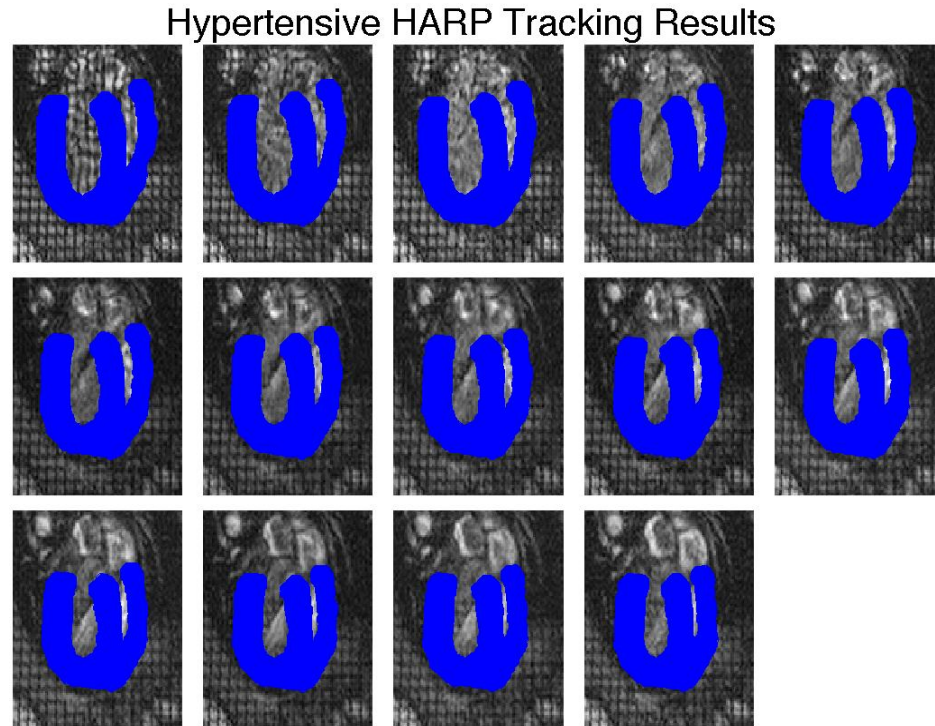


Figure 3-9: HARP tracking results for a hypertensive heart long axis slice. The top left represents the end-diastolic frame, while the bottom right is the end-systolic frame.

3.3 Three-Dimensional Strain Analysis

The strain distributions were calculated for both the control and hypertensive using the previously described techniques. Figure 3-10 represents end-systolic strain maps for the hypertensive and control heart. The maps show varying distributions of the LV and RV from apex to base and transmurally through the septal and lateral walls. All the strains varied between positive and negative values. Table 3-1 compares the end-systolic strains between the hypertensive and control hearts to published literature values. The basal and apical locations correspond to the elements on the top and bottom of the models respectively. Strain distributions were also calculated from end-diastole to end-systole. We first calculate the strain map distributions for each strain component from

end-diastole to end-systole (see Figure 3-11 for an example). We average the strain component values for specific regions (apex, base, etc.) and plot the change in strain over time (see Figure 3-12). The circumferential (E_{cc}) and longitudinal strain (E_{ll}) was similar and decreased in the hypertensive heart, respectively, which is consistent with published literature [26, 45]. The radial strain (E_{rr}) decreased in LV free wall and septum, and consistent in the RV. However, peak systolic E_{cc} and E_{rr} were slightly lower in magnitude compared to published results [16, 35, 45]. The fiber strain (E_{ff}) was fairly consistent between the two hearts except near the inferior LV wall where the strain was much lower in the hypertensive heart. Sheet-normal strain (E_{ss}) varied in all regions, as there was no discernable pattern. There was a strong decrease in the strain in the hypertensive RV apex and increased values in the LV mid wall. Cross-fiber strain (E_{nn}) was consistent some regions of the LV and RV free wall, but mostly varied across all regions. The LV base and equatorial areas had different patterns. Cross-fiber shortening has been associated with increased wall thickening [27] and this is present in some areas in the hypertensive heart, however not definitively. It is important to note that only one control and hypertensive model was used to calculate the strain component distributions, and because this low number of samples, it is difficult to draw major conclusions.

However, we have shown that these methods can determine accurate smooth strain maps.

From Figure 3-12, we can see notable differences between the hypertensive and control heart. Our goal was to determine if there was a correlation between regional differences in the cardiac geometry (wall thickness), fiber architecture, and strain. We selected areas of similar strain and different strains and plotted those values versus differences in wall thickness in the same regions. We also performed the same

measurement, but versus fiber overlap between the control and hypertensive model to determine if the difference in fiber architecture could account for differences in strain. We performed this on every strain component (see Figure 3-13 and 3-14 for an example). We determined that there was no significant correlation between differences in wall thickness and differences in strain, however there might be a slight correlation between overlap and strain differences, in which low overlap corresponds to high strain differences.

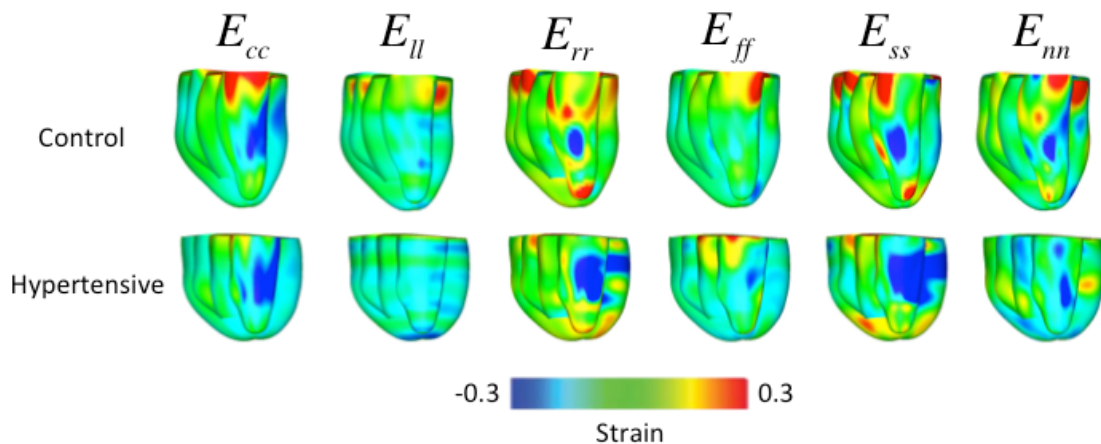


Figure 3-10: Multiple end-systolic strain maps that include circumferential (E_{cc}), radial (E_{rr}), longitudinal (E_{ll}), fiber (E_{ff}), sheet-normal (E_{ss}), and cross-fiber (E_{nn}) for the control and hypertensive model

Table 3-1: Three-Dimensional Strain Components in the LV and RV for the Control and Hypertensive Hearts compared to Published Values

	Control	Hypertensive	Koshizuka [45] (Rat control)	Koshizuka [45] (Rat hypertensive)	Saitta [39] (Human control)	Saitta [39] (Human hypertensive)	MacGowan [40] (Human control)	Injels [46] (Dogs control)
E_{cc}	-0.32	-0.33	-0.35	-0.35	-0.20	-0.22	N/A	-0.3
E_{ll}	-0.16	-0.14	-0.26	-0.21	-0.20	-0.15.9	N/A	-0.05
E_{rr}	0.17	0.3	0.41	0.35	0.54	0.40	N/A	0.4
E_{ff}	-0.15	-0.18	N/A	N/A	N/A	N/A	-0.14	-0.12
E_{ss}	0.06	0.06	N/A	N/A	N/A	N/A	N/A	0.08
E_{nn}	-0.16	-0.13	N/A	N/A	N/A	N/A	-0.08	-0.09

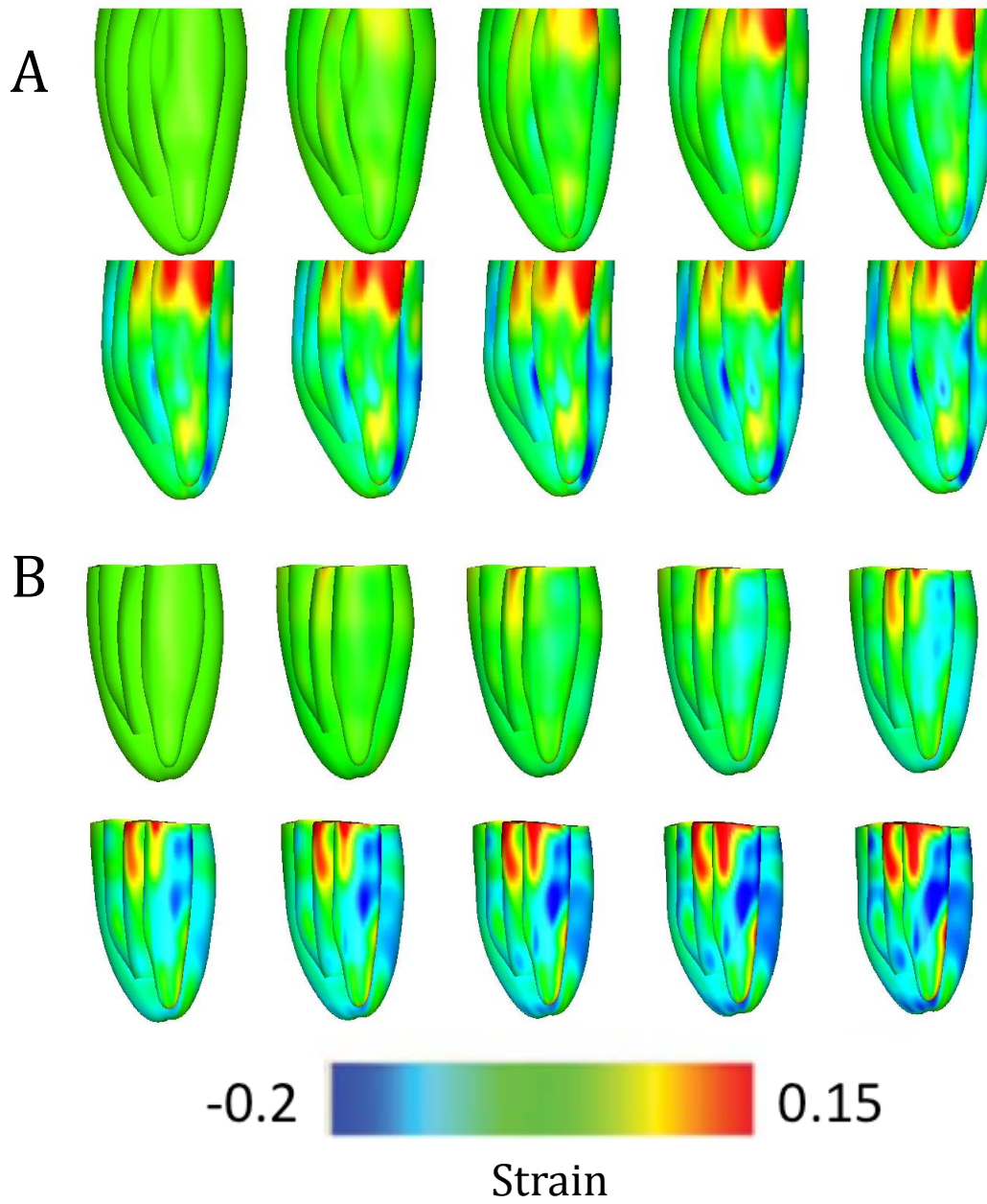


Figure 3-11: Fiber Strain Distribution maps from end-diastole to end-systole for the (A) Control and (B) Hypertensive models

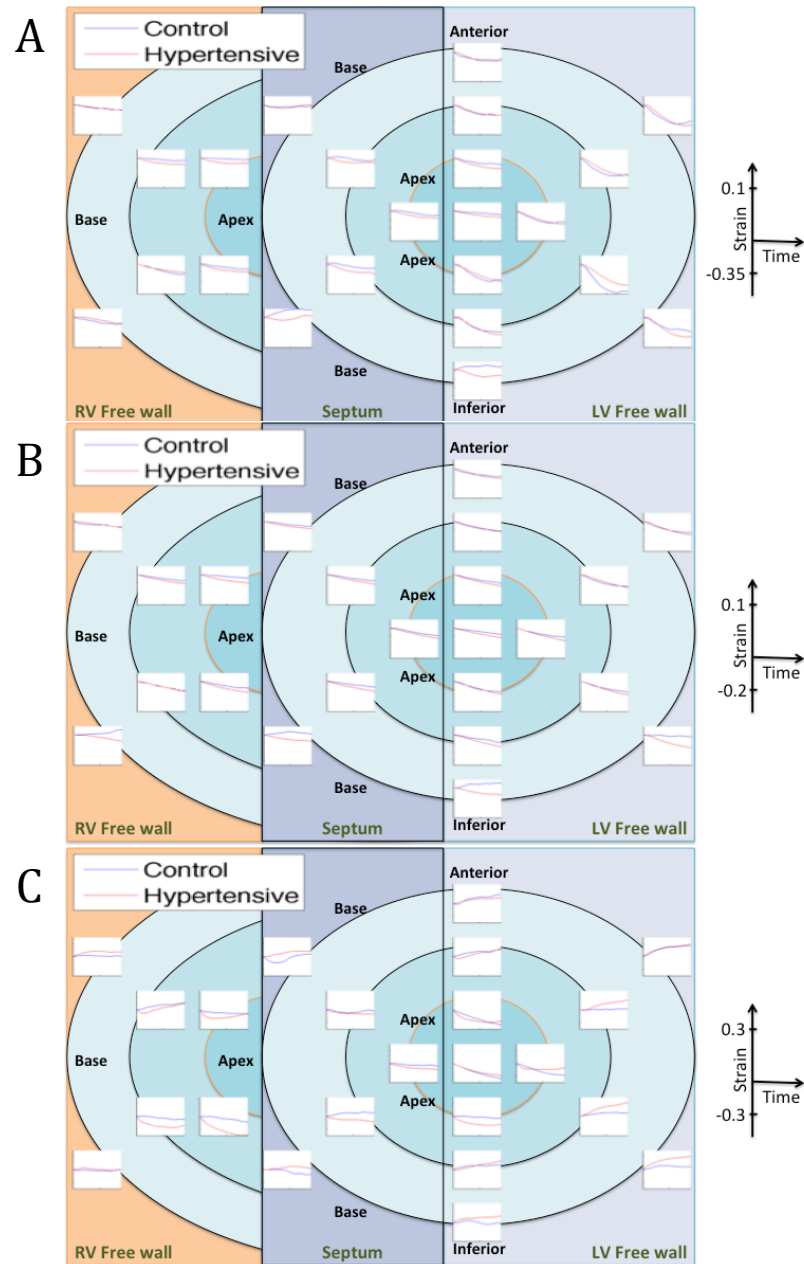


Figure 3-12: (A) Circumferential Strain distribution time courses from end-diastole to end-systole for the control and hypertensive heart (B) Longitudinal Strain distribution time courses from end-diastole to end-systole for the control and hypertensive heart (C) Radial Strain distribution time courses from end-diastole to end-systole for the control and hypertensive heart

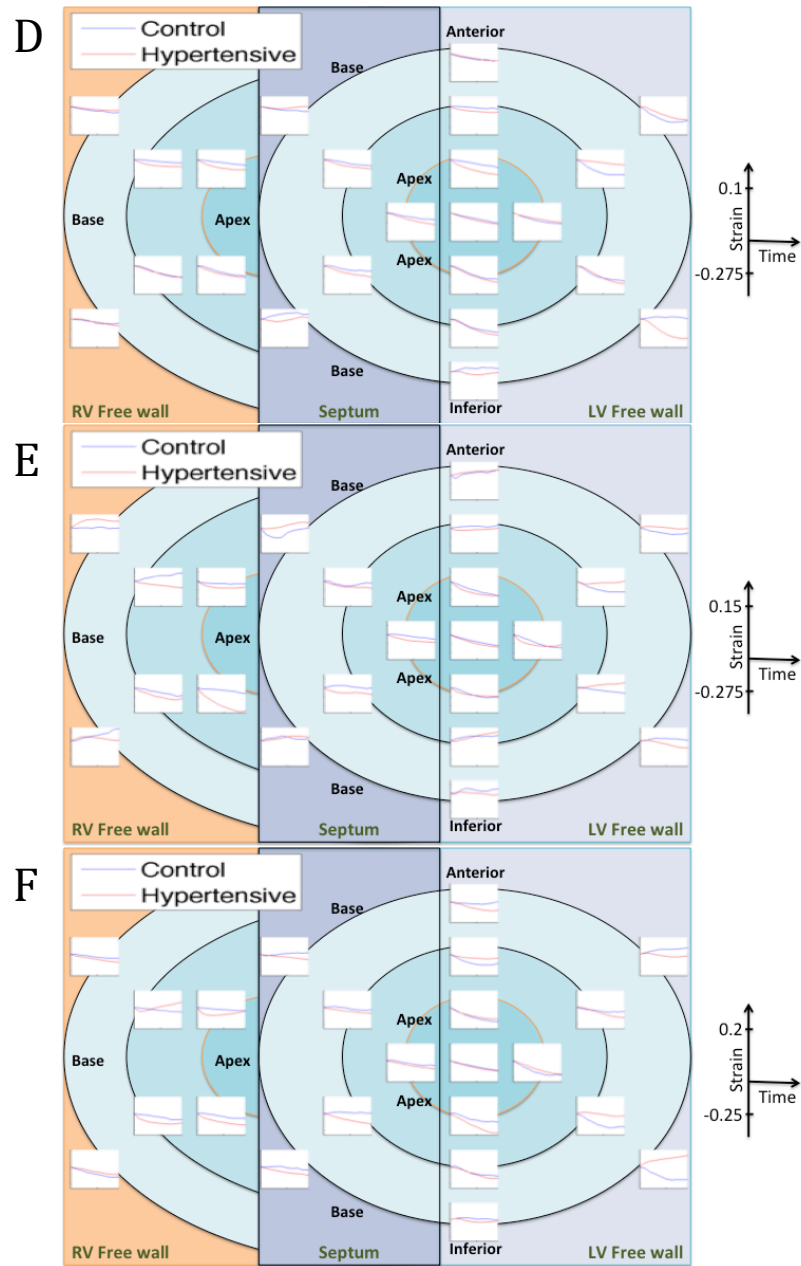


Figure 3-12: (D) Fiber Strain distribution time courses from end-diastole to end-systole for the control and hypertensive heart (E) Sheet-normal Strain distribution time courses from end-diastole to end-systole for the control and hypertensive heart (F) Cross-Fiber Strain distribution time courses from end-diastole to end-systole for the control and hypertensive heart, cont.

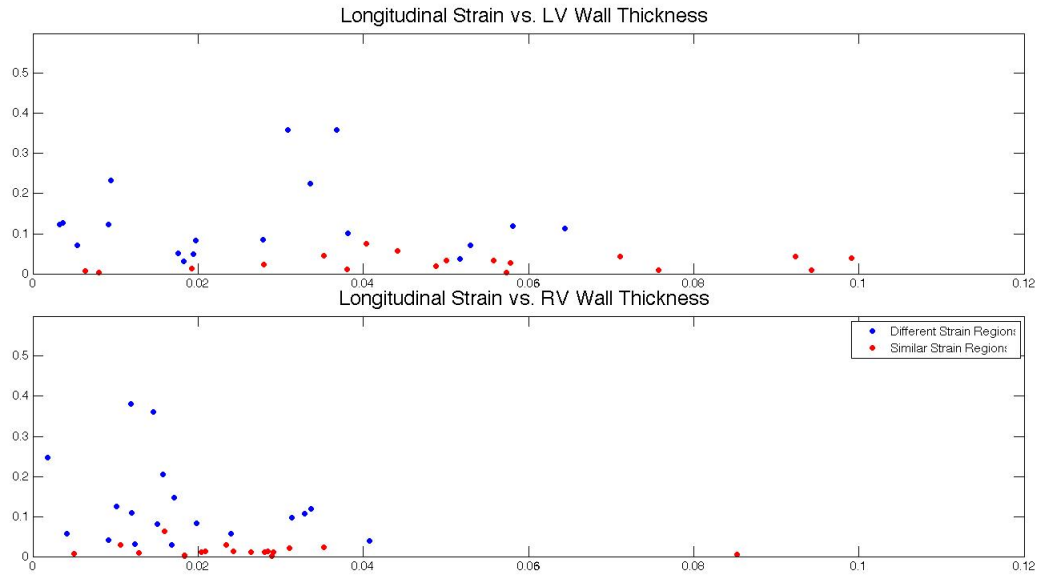


Figure 3-13: Longitudinal strain differences vs. Wall thickness differences for different regions in the LV and RV

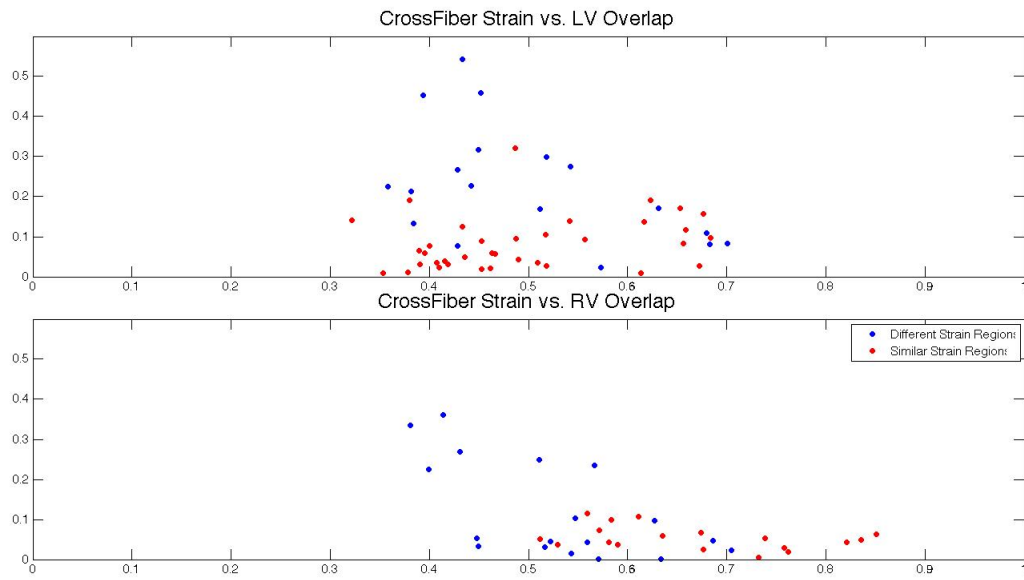


Figure 3-14: Cross-fiber strain differences vs. fiber overlap for different regions in the LV and RV

3.4 Preliminary Simulation Results

The end-diastolic meshes were used to simulate a contraction from end-diastole to end-systole and we measured ejection fraction as well as compared pressure curves to raw hemodynamics. Table 3-2 represent the parameters used for the simulations for both the control and hypertensive heart.

Table 3-2: Windkessel Paramaters for Simulations

	R (kPa*s/ml)	Z (kPa*s/ml)	C (ml/kPa)	Length of systole (s)	Cardiac Cycle time (s)
Control	160	573	0.00367	112	160
Hypertensive	160	1500	0.00367	119	154

We compared the aortic and LV pressure curves to the simulated curves (see Figure 3-15 and 3-16). It can be seen that these curves seemingly agree with each other. However, the simulated ejection fraction was too small (7%) compared to the measured ejection fraction from the MRI images (~70%). The difference in ejection can be explained by the extremely elevated resistance value, R , used in the simulations. We used a value ten times higher than literature values and the compliance, C , was also decreased by a factor of ten. These values were set in order to generate the appropriate pressure curves, but they did not simulate an accurate stroke volume. Stroke volume is inversely proportional to R , therefore this value must be decreased in order to achieve the accurate ejection fraction, however in our simulations, decreasing R plummeted the pressure, therefore, additional modification to other parameters is needed in order to simulate the ventricular contractions correctly.

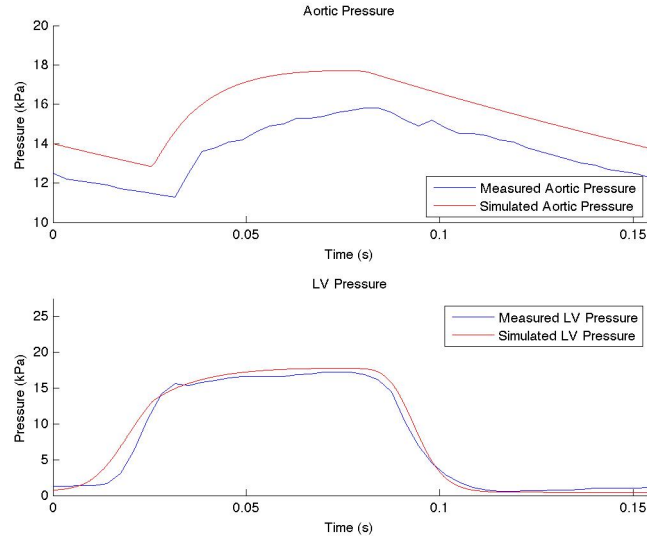


Figure 3-15: Simulation Results for the control heart, comparison between aortic (Top) and LV (Bottom) pressure and simulation results

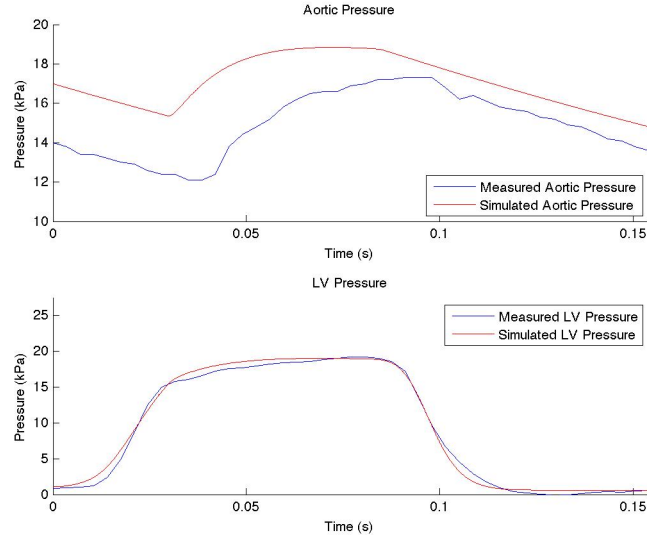


Figure 3-16: Simulation Results for the control heart, comparison between aortic (Top) and LV (Bottom) pressure and simulation results

4 Discussion

Previous studies measuring strain have focused on either echocardiographic or tagged MRI measurements to calculate two-dimensional deformation. Here, we have shown the ability to combine both HARP and finite element modeling to calculate more complete three-dimensional strain distributions. The goal of this thesis was to determine if these methods could accurately determine many different strain components and compare the values to published literature. In the future, these models can serve as validation tool for contraction simulation experiments. We have shown some preliminary simulation results that are promising, but require further optimization in order to predict accurate regional function in both hypertensive and normal rat hearts.

4.1 HARP Algorithm

HARP was utilized for material point tracking of the tagged MRI images. The procedure shown here combines a multitude of different published methods [1, 2, 3, 4, 5, 6, 7] in order to accurately track the myocardium. HARP has been mainly used to track

the LV wall, but we have shown that this method is powerful enough to track the RV as well with high accuracy. Tracking of the RV wall has been proven difficult due to its thin wall [36]. Therefore, a very small tagging grid and a high of frames are necessary in order to correctly track the RV, however this will increase scan times and cost. However, we have shown that by combining different aspects of HARP, we can track the RV wall. Unlike other tracking methods, HARP is an automatic tracking technique, which reduces processing time substantially. Errors occur when the deformation is the large between frames violating the small deformation assumption, however these errors can be reduced using SP-HARP [3]. This method allows large deformation points to be tracked accurately by improving the initial condition of each point by relating it to the seed voxel. This allows each point to converge to its correct location at a later time frame. Even though, the combination of SP-HARP and the standard HARP method allow for accurate tracking of material points, there are still errors due to the points moving out of the image plane. This results in mis-tracked points in one frame and unable to recover in later frames. In order to account for these errors, Prince et al. [6] developed a method that uses anisotropic diffusion smoothing to correct the mis-tracked points. Essentially, the technique involves smoothing the deformation gradient of each frame to correct the material points. HARP is also a very advantageous tool, as we are not limited by the image resolution, as interpolation is required to improve the displacement measurements for each material point. Therefore, we can define any number of material points for each image and track them over time. However, even though this technique is very powerful the tagging grid was large (1.8 mm) as compared to published values ($0.9\text{-}1.2\text{ mm}$). With a lower tagging resolution, the spectral peaks in k-space are closer together. Therefore if

the band pass filter is too large, there will be interference from other spectral peaks, especially the center peak. If the filter is too small, motion information could be lost. However, if the tagging resolution is too high, the HARP algorithm will be more sensitive to deformation, therefore in order to maximize the efficiency of HARP, one should use a high tagging and temporal resolution. CSPAMM imaging could have been used to improve the HARP analysis [17], which reduces noise from the central peak, but this method suffers from long scan acquisitions times and large cost.

4.2 Anatomical Model

We used existing techniques [9, 18] to accurately create finite element models of a normotensive and hypertensive heart by combining results from anatomical MRI images and DT-MRI measurements. The MRI images were used to accurately model the cardiac geometry while the DT-MRI measurements were used to calculate the fiber architecture of the heart. The anatomical images were used to accurately represent the cardiac geometry by fitting a three dimensional deformable model. The procedure involved registering MRI slices of different orientations together and fitting the model to the segmented surfaces (LV, RV, EPI, Septum). In order to properly register the short axis and the long axis images, we used a combination of image acquisition parameters. We had the spatial location of the first pixel of each image as well as the coordinate system of the image. Using this information as well as the matrix size and FOV, we can find the spatial location of each pixel referenced to the MRI scanner coordinate system. Now that we have the spatial locations of each image, we can register the short axis and

long axis scans together. However, this method assumes that the rat didn't move during the scan acquisition.

The fiber orientations were calculated for excised hearts and were able to be mapped to the end-diastolic ventricular models. Ideally, one would be able to perform *in vivo* cardiac DT-MRI calculations on the rat hearts so that they fiber warping would not be necessary. Previous studies have performed *in vivo* DT-MRI on human hearts [30, 31], but none have been performed on rat hearts. Overall, we have shown methods that can create an adequate representation of normal and diseased hearts.

4.3 Deformation Calculations

A deformable three-dimensional model was used to calculate strain distribution throughout the LV and RV wall. By combining the HARP results and the models, we were able to fit the models to each frame and simulate a heart contraction. Using this information, we measured strain time course maps from end-diastole to end-systole. We calculated circumferential, radial, and longitudinal strains using previously existing techniques [18]. E_{rr} decreased in the hypertensive model and E_{ll} also decreased suggesting increased shortening, which is consistent with literature results [45]. Our peak systolic E_{cc} was consistent with Vallee et al. [17] (-0.29 vs. -0.31). Control peak E_{rr} was low compared to published results (0.17 vs. 0.32) [37], however hypertensive peak E_{rr} was consistent (0.3 vs. 0.32). E_{ll} shortening was consistent compared to Adam et al. (-0.16 vs. -0.12) [42], but higher then compared with Waldman et al. (-0.16 vs. -0.1) [38], and lower compared to Koshizuka et al. (-0.16 vs. -0.26) . We compared our control and hypertensive heart results to published human control and hypertensive hearts. Peak

systolic E_{rr} , and E_{ll} in the control hearts were all low in comparison to the healthy human hearts, respectively (0.17 vs. 0.54, -0.16 vs. -0.20) [45], however peak E_{cc} was larger (-0.32 vs. -0.20) [39]. The hypertensive E_{cc} was much larger compared to human hypertensive hearts, while E_{rr} was low, however E_{ll} was consistent, respectively (-0.33 vs. -0.19, 0.3 vs. 0.57, -0.14 vs. -0.16) [39].

While many studies limited their strain calculations to circumferential, longitudinal, and radial strain [18, 20, 21, 26], we have shown the capabilities to calculate fiber, sheet-normal, and cross-fiber strains for both the LV and RV. Our E_{ff} and E_{nn} were higher to published healthy human hearts, respectively (-0.15 vs. -0.14, -0.16 vs. -0.08) [40]. E_{ss} was also low consistent to the results by Ingels Jr. [46] (0.06 vs. 0.08) in dogs, but E_{ff} and E_{nn} had higher shortening, respectively (-0.15 vs. -0.12, -0.16 vs. -0.09) [46]. While these methods have reproduced consistent and different results, they have proven to be able to calculate many different strain components. While we did not show any significant difference in the hypertensive heart, these techniques may be utilized to calculate accurate three dimensional strain distributions. We must reiterate that our sample size is very low and therefore, it is difficult to draw major conclusions. Ideally, we would want a larger sample size in order to measure different possible variations. Strain calculations could be improved with acquisition of additional short axis and long axis slices. Here, we only collected eight short axis slices and one long axis slice, which is not sufficient to fully describe the deformation of the heart.

The use of tagged MRI images to characterize RV strains has not been fully described in literature for rats. There have been some studies that have measured RV longitudinal strain using two-dimensional approaches [34]. Here, we show the power of

HARP and finite element modeling to measure RV strain. Our control RV E_{ll} compared to human results were lower (-0.09 vs. -0.21) [41]. RV strain is important measurement as previous studies have shown that it can be an indicator of pulmonary hypertension [32]. RV longitudinal strain has also been shown to quantify contractile function [33]. Hence, the ability to measure the RV strain maps can be utilized to serve as an indicator for right ventricular heart diseases.

While these models are useful for characterizing strain distribution maps, the future objective is the ability to simulate a rat heart contraction. We have shown preliminary simulation results for both the hypertensive and control hearts, and while the LV and aortic pressure curves correlate well with the raw hemodynamics, the expected ejection fraction was much too low (~7% vs. 70%). The low ejection can be explained by the elevated R value used. R is inversely proportional to the stroke volume (SV) and we can calculate R by using the following equation:

$$R = \frac{MAP}{SV} \cdot BCL \quad [4-1]$$

where,

MAP = Mean Arterial Pressure

SV = Stroke Volume

BCL = Length of Cardiac Cycle

Using this equation, we calculated R for a given SV, and using the previously described method, we calculated C . However, when these values were used, the peak LV pressure

and aortic pressure plummeted. Therefore, R was increased by a factor of ten and C was decreased by a factor of ten to maintain the time constant $\left(\frac{1}{RC}\right)$. Using these adjusted parameters, we achieved the results that have been shown previously. Further improvement must be made in order to accurately simulate the rat heart contraction. It is important to note that the passive material properties were not optimized for a rat heart and human heart model was used instead. In order to improve upon these results, R should decrease to its original value and other parameters in the active contraction model must be optimized.

5 Conclusion

Strain measurement techniques are increasing in popularity as more studies are showing that these quantities can be useful for diagnostic purposes. Therefore, optimizing current methods to accurately calculate strain components is paramount. Here, we have combined DT-MRI and MRI to create an accurate representation of the cardiac geometry and account for the fiber architecture. HARP analysis and finite element modeling techniques were used to measure three dimensional strain distributions. We have shown that this technique is capable of producing accurate results for both the LV and RV for our rat models. Preliminary simulation experiments were performed and showed promising results, but additional modification is needed in order to improve the

simulations. Overall, we have shown that three-dimensional strain maps can be accurately produced in for both the LV and RV of the rat heart. Using high-resolution structural mapping the strains can be found in terms of regional fiber architecture, providing detailed insight in myocyte fiber function in the rat heart, and also providing detailed regional function for future computational models of the contracting rat heart.

References

- 1) Osman, Nael F., William S. Kerwin, Elliot R. McVeigh, and Jerry L. Prince. "Cardiac Motion Tracking Using CINE Harmonic Phase (HARP) Magnetic Resonance Imaging." *Magnetic Resonance in Medicine* 42.6 (1999): 1048-060. Print.
- 2) Osman, Nael F., and Jerry L. Prince. "Imaging Motion Using Harmonic Phase MRI." *Imaging Motion Using Harmonic Phase MRI* 19.3 (2000): n. pag. Web
- 3) Liu, X., and J. L. Prince. "Shortest Path Refinement for Motion Estimation From Tagged MR Images." *IEEE Transactions on Medical Imaging* 29.8 (2010): 1560-572. Print.
- 4) Denney, Thomas S., Jr., Jin Li, and Craig A. Davis. "Analysis of Spectral Changes and Filter Design in Tagged Cardiac MRI." N.p., n.d. Web.
- 5) Barajas, Joel, Jaume Garcia-Barnes, Francesc Carreras, Sandra Pujadas, and Petia Radeva. "Angle Images Using Gabor Filters in Cardiac Tagged MRI." (n.d.): n. pag. Print.
- 6) Abd-Elmoniem, Khaled Z., Vijay Parthasarathy, and Jerry L. Prince. "Artifact Reduction in HARP Strain Maps Using Anisotropic Smoothing." *Medical Imaging* (2006): n. pag. Print.
- 7) Mattson, D. L. "Influence of Diet and Genetics on Hypertension and Renal Disease in Dahl Salt-sensitive Rats." *Physiological Genomics* 16.2 (2003): 194-203. Print.
- 8) Costandi, P. N., L. R. Frank, A. D. McCulloch, and J. H. Omens. "Role of Diastolic Properties in the Transition to Failure in a Mouse Model of the Cardiac Dilatation." *AJP: Heart and Circulatory Physiology* 291.6 (2006): H2971-2979. Print.
- 9) Krishnamurthy, Adarsh, Christopher T. Villongco, Joyce Chuang, Lawrence R. Frank, Jeffrey H. Omens, Roy C.P. Kerckhoffs, and Andrew D. McCulloch. "Patient-specific Models of Cardiac Biomechanics." N.p., n.d. Web.
- 10) Holzapfel, G. A., and R. W. Ogden. "Constitutive Modelling of Passive Myocardium: A Structurally Based Framework for Material

- Characterization." *Philosophical Transactions of the Royal Society A: Mathematical, Physical and Engineering Sciences* 367.1902 (2009): 3445-475. Print.
- 11) Lumens, Joost, Tammo Delhaas, Borut Kirn, and Theo Arts. "Three-wall Segment (TriSeg) Model Describing Mechanics and Hemodynamics of Ventricular Interaction." N.p., n.d. Web.
 - 12) Westerhof, Nico, Jan-Willem Lankhaar, and Berend E. Westerhof. "The Arterial Windkessel." *Medical & Biological Engineering & Computing* 47.2 (2009): 131-41. Print.
 - 13) Basser, Peter J. "Inferring Microstructural Features and the Physiological State of Tissues from Diffusion-weighted Images." *NMR in Biomedicine* 8.7 (1995): 333-44. Print.
 - 14) Yeo, B.t.t., T. Vercauteren, P. Fillard, J.-M. Peyrat, X. Pennec, P. Golland, N. Ayache, and O. Clatz. "DT-REFinD: Diffusion Tensor Registration With Exact Finite-Strain Differential." *IEEE Transactions on Medical Imaging* 28.12 (2009): 1914-928. Print.
 - 15) Klotz, S. "Single-beat Estimation of End-diastolic Pressure-volume Relationship: A Novel Method with Potential for Noninvasive Application." *AJP: Heart and Circulatory Physiology* 291.1 (2006): H403-412. Print.
 - 16) Hyacinthe, J.-N., M. K. Ivancevic, J.-L. Daire, and J.-P. Vallée. "Feasibility of Complementary Spatial Modulation of Magnetization Tagging in the Rat Heart after Manganese Injection." *NMR in Biomedicine* 21.1 (2008): 15-21. Print.
 - 17) Ivancevic, M. K., J-L. Daire, J-N. Hyacinthe, G. Crelier, S. Kozerke, K. Montet-Abou, and J-P. Vallee. "High-resolution CSPAMM Rat Heart Tagging on a 1.5T Clinical MR System." (n.d.): n. pag. Print.
 - 18) Chuang, Joyce S., Alice Zemljic-Harpp, Robert S. Ross, Lawrence R. Frank, Andrew D. McCulloch, and Jeffrey H. Omens. "Determination of Three-dimensional Ventricular Strain Distributions in Gene-targeted Mice Using Tagged MRI." *Magnetic Resonance in Medicine* 64.5 (2010): 1281-288. Print.
 - 19) "Human Heart Structure." *Human Heart Structure*. N.p., n.d. Web. 05 Dec. 2013.
 - 20) Saito, Makoto, Hideki Okayama, Toyofumi Yoshii, Haruhiko Higashi, Hiroe Morioka, Go Hiasa, Takumi Sumimoto, and Jitsuo Higaki. "Clinical Significance of Global Two-dimensional Strain as a Surrogate Parameter of Myocardial

- Fibrosis and Cardiac Events in Patients with Hypertrophic Cardiomyopathy." N.p., n.d. Web.
- 21) Holt, Brian D. "Strain and Strain Rate Echocardiography and Coronary Artery Disease." *Advances in Cardiovascular Imaging* (n.d.): n. pag. Print.
- 22) Gjesdal, O., E. Hopp, K. Lunde, T. Halle-Valle, and T. Edvardsen. "Global Longitudinal Strain Measured by Two-dimensional Speckle Tracking Echocardiography Is Closely Related to Myocardial Infarct Size in Chronic Ischaemic Heart Disease." N.p., n.d. Web
- 23) Fonseca, C., A. Dissanayake, R. Doughty, G. Whalley, G. Gamble, B. Cowan, C. Occleshaw, and A. Young. "Three-dimensional Assessment of Left Ventricular Systolic Strain in Patients with Type 2 Diabetes Mellitus, Diastolic Dysfunction, and Normal Ejection Fraction." *The American Journal of Cardiology* 94.11 (2004): 1391-395. Print.
- 24) D'hooge, J. "Regional Strain and Strain Rate Measurements by Cardiac Ultrasound: Principles, Implementation and Limitations." *European Journal of Echocardiography* 1.4 (2000): 295-99. Print.
- 25) Urheim, S., T. Edvardsen, H. Torp, and OA Smiseth. "Myocardial Strain by Doppler Echocardiography: Validation of a New Method to Quantify Regional Myocardial Function." N.p., n.d. Web.
- 26) Kouzu, Hidemichi, Satoshi Yuda, Atsuko Muranaka, Takahiro Doi, Hitomi Yamamoto, Shinya Shimoshige, Mamoru Hase, Akiyoshi Hashimoto, Shigeyuki Saitoh, and Kazufumi Tsuchihashi. "Left Ventricular Hypertrophy Causes Different Changes in Longitudinal, Radial, and Circumferential Mechanics in Patients with Hypertension: A Two-Dimensional Speckle Tracking Study." *Journal of the American Society of Echocardiography* 24.2 (2011): 192-99. Print.
- 27) Rademakers, FE, WJ Rogers, WH Guier, GM Hutchins, CO Siu, and EP Shapiro. "Relation of Regional Cross-fiber Shortening to Wall Thickening in the Intact Heart. Three-dimensional Strain Analysis by NMR Tagging." N.p., n.d. Web.
- 28) Daire, Jean-Luc, Jean-Pascal Jacob, Jean-Noel Hyacinthe, Pierre Croisille, Karin Montet-Abou, Sophie Richter, Diomidis Botsikas, Matthieu Lepetit-Coiffé, Denis Morel, and Jean-Paul Vallée. "Cine and Tagged Cardiovascular Magnetic Resonance Imaging in Normal Rat at 1.5 T: A Rest and Stress Study." *Journal of Cardiovascular Magnetic Resonance* 10.1 (2008): 48. Print.

- 29) Liu, Wei, Junje Chen, Songbai Ji, Stacy J. Allen, and Xin Yu. "HARP MRI Tagging for Direct Quantification of Lagrangian Strain in Rat Hearts After Myocardial Infarction." N.p., n.d. Web.
- 30) Reese, Timothy G., Robert M. Weisskoff, R. Niel Smith, Bruce R. Rosen, Robert E. Dinsmore, and Van J. Wedeen. "Imaging Myocardial Fiber Architecture in Vivo with Magnetic Resonance." N.p., n.d. Web.
- 31) Wu, M.-T., W.-Y. I. Tseng, M.-Y. M. Su, C.-P. Liu, K.-R. Chiou, V. J. Wedeen, T. G. Reese, and C.-F. Yang. "Diffusion Tensor Magnetic Resonance Imaging Mapping the Fiber Architecture Remodeling in Human Myocardium After Infarction: Correlation With Viability and Wall Motion." *Circulation* 114.10 (2006): 1036-045. Print.
- 32) Naderi, N., Z. Ojaghi Haghighi Z, A. Amin, F. Naghashzadeh, and M. Maleki. "Utility of Right Ventricular Strain Imaging in Predicting Pulmonary Vascular Resistance in Patients with Pulmonary Hypertension." N.p., n.d. Web.
- 33) Jamal, F., C. Bergerot, L. Argaud, J. Loufouat, and M. Ovize. "Longitudinal Strain Quantitates Regional Right Ventricular Contractile Function." N.p., n.d. Web.
- 34) Chow, P-C, X-C Liang, E W Y. Cheung, W W M. Lam, and Y-F Cheung. "New Two-dimensional Global Longitudinal Strain and Strain Rate Imaging for Assessment of Systemic Right Ventricular Function." *Heart* 94.7 (2008): 855-59. Print.
- 35) Liu, W., M. W. Ashford, J. Chen, M. P. Watkins, T. A. Williams, S. A. Wickline, and X. Yu. "MR Tagging Demonstrates Quantitative Differences in Regional Ventricular Wall Motion in Mice, Rats, and Men." *AJP: Heart and Circulatory Physiology* 291.5 (2006): H2515-2521. Print.
- 36) Shehata, Monda L., Susan Cheng, Nael F. Osman, David A. Bluemke, and João AC Lima. "Myocardial Tissue Tagging with Cardiovascular Magnetic Resonance." *Journal of Cardiovascular Magnetic Resonance* 11.1 (2009): 55. Print.
- 37) Fu, Y. B., C. K. Chui, and C. L. Teo. "Value of Segmental Myocardial Strain by 2-dimensional Strain Echocardiography for Assessment of Scar Area Induced in a Rat Model of Myocardial Infarction." N.p., n.d. Web.

- 38) Omens, Jeffrey H., DD Farr, Andrew D. McCulloch, and LK Waldman. "Comparison of Two Techniques for Measuring Two-dimensional Strain in Rat Left Ventricles." N.p., n.d. Web.
- 39) MImbalzano, Egidio, Concetta Zito, Scipione Carerj, Giuseppe Oreto, Giuseppe Mandraffino, Maurizio Cusmà-Piccione, Gianluca Di Bella, Carlo Saitta, and Antonino Saitta. "Left Ventricular Function in Hypertension: New Insight by Speckle Tracking Echocardiography." *Echocardiography* 28.6 (2011): 649-57. Print.
- 40) MacGowan, GA., EP. Shapiro, H. Azhari, CO. Siu, PS. Hees, GM. Hutchins, JL. Weiss, and FE. Rademakers. "Noninvasive Measurement of Shortening in the Fiber and Cross-Fiber Directions in the Normal Human Left Ventricle and in Idiopathic Dilated Cardiomyopathy." N.p., n.d. Web.
- 41) Taylor, Michael D., Kan N. Hor, Wojceich Mazur, Woodrow D. Benson, and William M. Gottliebson. "Right Ventricular Strain in Patients with Tetralogy of Fallot." (n.d.): n. pag. Print.
- 42) Bachner-Hinenzon, N., O. Ertracht, M. Leitman, Z. Vered, S. Shimoni, R. Beerli, O. Binah, and D. Adam. "Layer-specific Strain Analysis by Speckle Tracking Echocardiography Reveals Differences in Left Ventricular Function between Rats and Humans." *AJP: Heart and Circulatory Physiology* 299.3 (2010): H664-672. Print.
- 43) Ashikaga, H. "Transmural Left Ventricular Mechanics Underlying Torsional Recoil during Relaxation." *AJP: Heart and Circulatory Physiology* 286.2 (2004): 640H-47. Print.
- 44) Sosnovik, David E., Ruopeng Wang, Guangping Dai, Timothy G. Reese, and Van J. Wedeen. "Diffusion MR Tractography of the Heart." *Journal of Cardiovascular Magnetic Resonance* 11.1 (2009): 47. Print.
- 45) Koshizuka, Rumi, Tomoko Ishizu, Yuri Kameda, Ryo Kawamura, Yoshihiro Seo, and Kazutaka Aonuma. "Longitudinal Strain Impairment as a Marker of the Progression of Heart Failure with Preserved Ejection Fraction in a Rat Model." *Journal of the American Society of Echocardiography* 26.3 (2013): n. pag. Print.
- 46) Ashikaga, H. "Transmural Left Ventricular Mechanics Underlying Torsional Recoil during Relaxation." *AJP: Heart and Circulatory Physiology* 286.2 (2004): 640H-47. Print.